Nano-Micro Letters

ARTICLE

Absorption-Dominant mmWave EMI Shielding Films with Ultralow Reflection using Ferromagnetic Resonance Frequency Tunable M-Type Ferrites

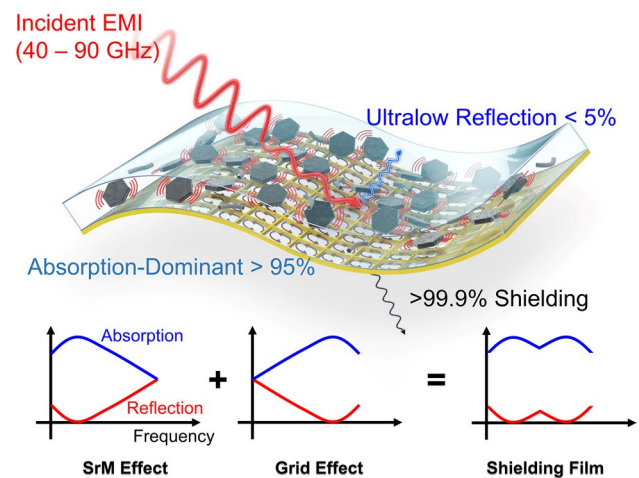Horim Lee[1], Seung Han Ryu[1], Suk Jin Kwon[1], Jae Ryung Choi[1], Sang-bok Lee[1], Byeongjin Park[1] ✉

HIGHLIGHTS

- A novel multi-band absorption-dominant electromagnetic interference (EMI) shielding film with transition metal-doped M-type strontium ferrites composite layer and a conductive grid is developed.

- This film shows (1) ultralow EMI reflection less than 5%, (2) in multiple mmWave frequency bands corresponding to ferrites and grid characteristics, (3) with a broadband EMI shielding performance over 99.9% from 40 to 90 GHz.

ABSTRACT Although there is a high demand for absorption-dominant electromagnetic interference (EMI) shielding materials for 5G millimeter-wave (mmWave) frequencies, most current shielding materials are based on reflection-dominant conductive materials. While there are few absorption-dominant shielding materials proposed with magnetic materials, their working frequencies are usually limited to under 30 GHz. In this study, a novel multi-band absorption-dominant EMI shielding film with M-type strontium ferrites and a conductive grid is proposed. This film shows ultralow EMI reflection of less than 5% in multiple mmWave frequency bands with sub-millimeter thicknesses, while shielding more than 99.9% of EMI. The ultralow reflection frequency bands are controllable by tuning the ferromagnetic resonance frequency of M-type strontium ferrites and composite layer geometries. Two examples of shielding films with ultralow reflection frequencies, one for 39 and 52 GHz 5G telecommunication bands and the other for 60 and 77 GHz autonomous radar bands, are presented. The remarkably low reflectance and thinness of the proposed films provide an important advancement toward the commercialization of EMI shielding materials for 5G mmWave applications.

Incident EMI (40 – 90 GHz)
Ultralow Reflection < 5%
Absorption-Dominant > 95%
>99.9% Shielding

Absorption / Reflection — Frequency — SrM Effect + Grid Effect = Shielding Film

KEYWORDS 5G communication; MmWave; EMI shielding; M-type ferrites

✉ Byeongjin Park, b.park@kims.re.kr
[1] Composites Research Division, Korea Institute of Materials Science, 797 Changwondaero, Seongsan-Gu, Changwon, Gyeongsangnam-Do 51508, Republic of Korea

1 Introduction

Although current 4G long-term evolution (LTE) telecommunication works in 2.1 GHz frequency bands, 5G telecommunication requires at least 10 times higher frequency bands over 26 GHz, commonly known as millimeter waves (mmWave, 30–100 GHz). Moreover, 5G telecommunication leads to more usage of electronic and telecommunication devices working in high- and multiple-frequency bands, including mobile phones (e.g., 26, 39, and 52 GHz) and autonomous vehicles (e.g., 60 and 77 GHz). This stimulates an increasing concern about electromagnetic interference (EMI) between these devices, which causes electronic malfunctions and even their complete failures [1, 2]. For example, EMI in autonomous vehicle radars may cause misdetection or false detection of targets and lead to severe accidents [3]. Thus, there is a high demand for (1) thin shielding materials, (2) working in mmWave, (3) with broadband/multiband shielding capability.

EMI shielding materials can be classified into reflection-dominant and absorption-dominant types according to the reflection and absorption contribution to the total shielding [4]. For previous generations of telecommunication, reflection-dominant shielding materials, including metal [2, 5–7], carbon nanotubes [8–12], graphene [13–15] and MXene-based [1, 16–19] materials, have been widely used with their high shielding effectiveness (SE) over 40 dB (99.99% EMI shielding). Due to their high conductivity, they can effectively reflect more than 90% of the external EMI ($\geq$ 10 dB reflection shielding effectiveness (SER)) and minimize its transmission even as a thin film less than 20 μm thickness. However, the reflected EMI may cause secondary radiation pollution, which generates additional superposition and interference with other electromagnetic waves. This is a more serious issue with a short wavelength of 5G mmWave frequency bands and tight component-to-component spacing in integrated 5G mobile modules [20]. Therefore, there is a high demand for absorption-dominant 5G EMI shielding materials with low reflection and high absorption of EMI [21–23]. The SER of absorption-dominant shielding materials should not be higher than 3 dB as it will reflect more than 50% of EMI [24].

To solve this problem, there have been several studies on absorption-dominant shielding materials working at mmWave frequency bands. Although each approach has its own advantages, most of the literature is limited to the 26 GHz 5G band [25–30], and absorption-dominant shielding materials for mmWave over 40 GHz are rarely reported [31, 32, 33, 34]. Foam materials are widely known to be very effective absorption-dominant materials due to their well-matched impedance to air [25, 27, 28, 34]. Zhao et al. reported a 4 mm thick PVDF/multiwall carbon nanotube (MWCNT) foam with 17.1 dB SE and 1.6 dB SER (31% reflection) at 40 GHz [34]. However, due to the high void content of foam materials, their thickness usually needs to be more than several millimeters to achieve satisfactory SE over 20 dB (99% EMI shielding), which limits their application to mobile electronics. Though Ma et al. proposed an interesting multilayer structure with a conductive film and a porous foam to achieve a high SE of 32.6 dB and ultralow SER of 3.1×10^{-4} dB (0.7% reflection) with reduced material thickness, its thickness is still 1.95 mm for Ku-Band (12–18 GHz) applications [35]. Magnetic material-based composites have also been of interest due to their low conductivity and high magnetic loss [26, 36]. There have been various attempts to increase the magnetic loss of magnetic materials including one-dimensional magnetic chain [37–39], core–shell structures [40–43], and regulated structural defects [44]. However, as most common magnetic materials, e.g., Fe or Co, lose their magnetic characteristics over 30 GHz, their EMI shielding performance is usually unsatisfactory in mmWave frequency bands. Zhang et al. proposed an AlCoCrFeNi alloy composite working at 40 GHz with a 1 dB SER (20% reflection) and 2 mm thickness; however, its SE was limited to 15 dB [31]. Although the authors' group attempted to improve the SE over 20 dB and minimize the SER below 0.5 dB (10% reflection) at 0.4 mm thickness with Fe composites and conductive grids, these applications are still limited to 26 GHz [29, 30].

Recently, M-type ferrite has been widely investigated as an effective EMI shielding material for mmWave frequency bands [45, 46]. Ferromagnetic materials are known to exhibit high magnetic loss at a specific frequency band via ferromagnetic resonance (FMR). While most soft magnetic materials (e.g., Fe and Co) and ferrites (e.g., spinel, garnet, W-, X-, Y-, and Z-type) have a low FMR frequency below several GHz, M-type ferrite can induce FMR at over 45 GHz due to its higher magnetic anisotropy than other magnetic materials [47]. Since it is known that the FMR frequency of M-type ferrite is proportional to the magnitude of magnetic anisotropy, the concept of changing its magnetic anisotropy to control the FMR frequency band has received
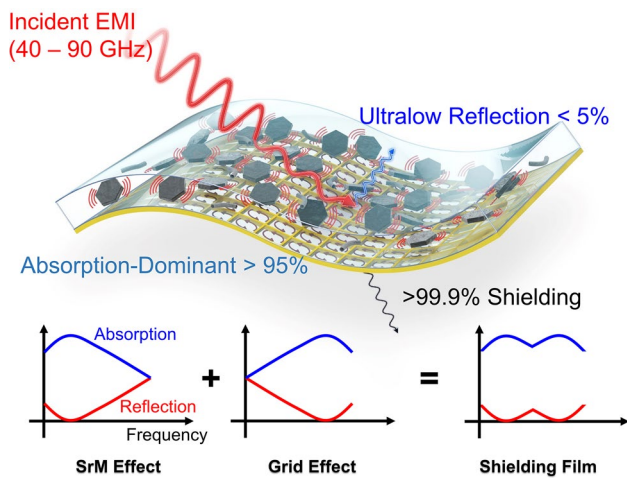
Fig. 1 Schematic diagram of the proposed shielding film with a transition metal-doped M-type strontium ferrites composite layer and a conductive grid

much attention from many researchers [48]. In particular, the substitution of Fe^{3+} ions constituting M-type ferrite into various transition metal ions is considered an effective method to change the magnetic properties of M-type ferrite [49–60]. For example, $Co^{2+}Ti^{4+}$ and Al^{3+} are known to be effective elements to decrease and increase magnetic anisotropy, respectively [59, 61]. However, there has been few reports on relating the effect of ion substitution, magnetic anisotropy change, and the FMR frequency shift in mmWave frequency bands [52–55]. In addition, as FMR occurs at a specific frequency band, it is difficult to achieve broadband or multi-band EMI shielding performance using M-type ferrites only.

In this study, a novel multi-band absorption-dominant EMI shielding film with transition metal-doped M-type strontium ferrites (SrMs) is proposed (Fig. 1). This film shows (1) ultralow EMI reflection less than 5% (0.1 dB SER), (2) in multiple mmWave frequency bands, (3) with a broadband EMI shielding performance over 30 dB SE (99.9% EMI shielding) from 40 to 90 GHz. By integrating a SrM composite layer and a conductive Cu grid, ultralow SER and high SE are simultaneously achieved with sub-millimeter thicknesses. The ultralow reflection frequency bands are controllable by tuning the FMR frequency of the SrM and composite layer dimensions, and a transmission line model is proposed for the theoretical design of the shielding films. Two examples of the proposed shielding films are presented: one for 39 and 52 GHz 5G telecommunication bands and the other for 60 and 77 GHz

autonomous radar bands. For both applications, the shielding films show less than 5% ultralow EMI reflection at the desired multiple frequency bands while shielding 99.9% EMI with 0.58 and 0.34 mm thicknesses, respectively. To the best of the authors' knowledge, this is the first reported absorption-dominant mmWave shielding material for multiple frequency bands.

This paper is organized as follows. First, a FMR frequency tunable SrM is introduced, and its magnetic characteristics are discussed. Second, the design factors for the proposed EMI shielding films are explained with a transmission line model. Then, two examples of shielding films are presented with measured a SE and compared with transmission line model predictions. The shielding performance of the proposed shielding films is also compared with previously reported literature.

2 Experimental

2.1 Materials

The precursors used for doped SrMs were strontium nitrate $(Sr(NO_3)_2)$, iron nitrate nonahydrate $(Fe(NO_3)_3 \cdot 9H_2O)$, cobalt nitrate hexahydrate $(Co(NO_3)_2 \cdot 6H_2O)$, titanium isopropoxide $(Ti(OCH(CH_3)_2)_4)$, aluminum nitrate nonahydrate $(Al(NO_3)_3 \cdot 9H_2O)$ and citric acid monohydrate $(C_6H_8O_7 \cdot H_2O)$. All the chemicals were purchased from Sigma−Aldrich and used as received without any further purification. A thermoplastic polyurethane (TPU) solution, 30 wt% TPU dissolved in n,n-dimethylformamide (DMF), from Songwon Industrial, Korea, was used as a polymer binder for the magnetic composite layer. Single-walled carbon nanotube (CNT, JENO 8A) from JEIO Co., Korea is used to control permittivity of the composite layer. A Cu grid, designed by the authors, was manufactured by Samwon ACT, Korea via electroforming.

2.2 Preparation of the M-type Strontium Ferrites

Co-Ti and Al doped SrMs powders $(SrFe_{12-2x}Co_xTi_xO_{19}$ and $SrFe_{12-x}Al_xO_{19})$ were synthesized using the citrate sol–gel method. First, stoichiometric quantities of strontium nitrate, iron nitrate nonahydrate, cobalt nitrate hexahydrate, titanium isopropoxide, aluminum nitrate nonahydrate and citric acid monohydrate were dissolved in deionized water. The concentration of Sr^{2+} ions was

0.05 M, and the molar ratio of Sr^{2+} ion: citric acid monohydrate was 1:1. Then, the mixed solution was heated to 90 °C for 24 h to completely evaporate the water. Afterward, the dried gel was gently hand-ground using a mortar with 40 wt% NaCl and calcined at 1,250 °C for 3 h. Finally, the calcined powder was washed 5 times with deionized water to remove residual NaCl and dried at 80 °C for 24 h.

2.3 Preparation of the EMI Shielding Films

A TPU solution and SrMs were mixed with a weight ratio of TPU:SrMs = 3:7 using a planetary mixer (ARE-310, Thinky) for 5 min at 2,000 rpm. A desired fraction of CNT (0.1–0.5 wt%) was mixed together with SrM and TPU only when a higher permittivity of the composite layer is needed. The mixed composite solution was cast into 100 μm thick layers via bar coating. The casted layers were dried for 30 min at 110 ℃ to evaporate unnecessary DMF solvents in the composite layers. Finally, stacked composite layers, with a Cu grid at the bottom, were pressed at 120 ℃ with 10 MPa for 20 min to prepare a shielding film of desired thickness using a thickness gauge.

2.4 Material Characterizations

The morphologies of doped SrM powders and proposed EMI shielding films were analyzed using a scanning electron microscope (JSM-7001F, JEOL) and a transmission electron microscope (JEM-F200, JEOL). The crystal structures of the doped SrM powder were analyzed by X-ray diffraction (D/Max 2500, RIGAKU) with Cu Ka radiation. The Rietveld refinement of XRD data was performed by Fullprof Suite software package to verify the crystal structural analysis. X-ray photonelectron spectrometer (AXIS SUPRA, Kratos) were used to study the chemical bonding and the valence state. The magnetic hysteresis loops were measured using a vibrating sample magnetometer (EZ9 VSM, Microsense) with an applied field of ± 20 kOe.

To obtain the shielding effectiveness of the products, a vector network analyzer (N5291A, Keysight) and a free space measurement system (FS-110, EMLabs) were used for scattering the parameter measurements. Scattering parameters were measured in four different frequency bands: the R (26.5–40 GHz), Q (33–50 GHz), V (50–75 GHz), and W (75–110 GHz) bands. The samples were prepared by cutting

the EMI shielding film into rectangular specimens of 10×10 cm^2. The shielding effectiveness and shielding efficiency were calculated from the measured scattering parameters as follows:

$$R = \left| S_{11} \right|^2 \tag{1}$$

$$T = \left| S_{21} \right|^2 \tag{2}$$

$$A = 1 - R - T \tag{3}$$

$$SER = -10\log(1 - R) \tag{4}$$

$$SEA = -10\log(T/(1 - R)) \tag{5}$$

$$SE = SER + SEA \tag{6}$$

where S_{11} and S_{21} refer to the scattering parameters; SER, SEA, and SET are the shielding effectiveness of relfection, absorption, and total; and R, T, and A refer to the reflectance, transmittance, and absorbance, respectively, which are also known as shielding efficiency. R and A can be also calculated from SE as follows, from Eqs. (4) and (5):

$$R = \left(1 - 10^{-\frac{SER}{10}} \right) \tag{7}$$

$$A = \left(1 - 10^{-\frac{SEA}{10}} \right) \times (1 - R) \tag{8}$$

The electromagnetic parameters (complex permeability and permittivity) of the composite layer were also obtained using the aforementioned measurement system. These parameters are calculated from the measured scattering parameters using the Nicholson–Ross–Weir method [62].

3 Ferromagnetic Resonance Frequency Tunable M-type Strontium Ferrites

3.1 Microstructure of Doped M-type Strontium Ferrites

Figure 2 displays the refined XRD patterns of pure ($SrFe_{12}O_{19}$) SrM, Co–Ti doped SrM, and Al doped SrM powder, respectively. The XRD data of all synthesized SrM samples were analyzed using the Rietveld refinement process with the Fullprof suite software package. As depicted in Fig. 2, all diffraction peaks are indexed to a single phase of
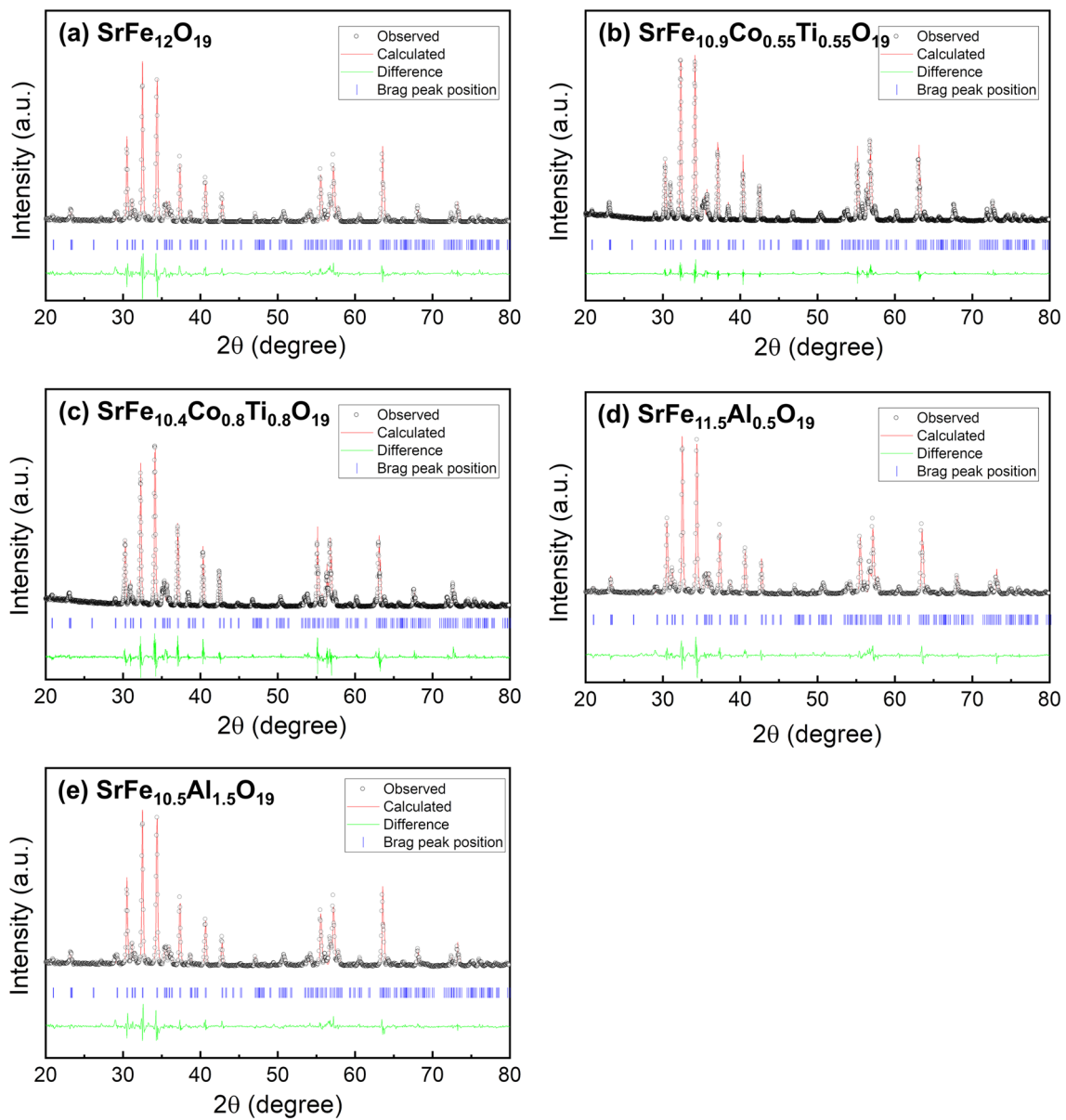
Fig. 2 Refined X-ray diffraction patterns of **a** pure SrM, **b, c** Co–Ti doped SrM, and **d, e** Al doped SrM powder

Table 1 Calculated lattice constants of doped SrMs and obtained fitting parameter value

Composition	Lattice constants			R-factors		
	a (Å)	c (Å)	V (Å)	R_p (%)	R_{wp} (%)	χ^2
$SrFe_{12}O_{19}$	5.889	23.086	693.742	20.0	26.5	1.29
$SrFe_{10.9}Co_{0.55}Ti_{0.55}O_{19}$	5.889	23.086	693.826	20.8	20.3	0.946
$SrFe_{10.4}Co_{0.8}Ti_{0.8}O_{19}$	5.890	23.065	693.430	22.0	23.2	1.20
$SrFe_{11.5}Al_{0.5}O_{19}$	5.864	22.931	683.481	18.5	18.2	0.917
$SrFe_{10.5}Al_{1.5}O_{19}$	5.851	22.902	679.520	18.9	19.3	1.002

the M-type hexagonal structure with P63/mmc space group. Furthermore, the experimental results for all samples agreed well with the corresponding simulated XRD pattern, as evidenced by the high goodness of fit parameters χ^2, as shown in Table 1. These outcomes support the conclusion that the Fe sites of $SrFe_{12}O_{19}$ were successfully substituted by Co–Ti and Al atoms for all dopant concentrations without any secondary phase.

Table 1 also presents the lattice constants calculated from the refined XRD pattern. The lattice constant of Co–Ti doped SrMs remained unchanged with varying doping concentrations, whereas the lattice constant of Al doped SrMs decreased with increasing doping concentration. This phenomenon could be attributed mainly to the distinct ionic radii of Co^{2+}, Ti^{4+}, and Al^{3+}. The ionic radii of Co^{2+} and Ti^{4+} are 0.745 and 0.605 Å, respectively, resulting in an average radius of 0.675 Å for co-substitution, which is comparable to the Fe^{3+} ion's radius of 0.645 Å. On the other hand, the ionic radius of Al^{3+} is 0.535 Å, which is only 83% of the Fe^{3+} ionic radius, leading to a shrinkage of the crystal lattice.

Figure 3 illustrates the SEM images of the pure, Co-Ti doped, and Al doped SrM powders with different doping concentrations. All samples were calcined at 1250 °C for 3 h in molten NaCl flux for rapid mass diffusion, which facilitated crystal growth. Interestingly, Co–Ti doped SrM powders show a well-shaped hexagonal plate-like structure, and Al doped SrM powders show smaller particle sizes than pure SrM powders.

High-resolution TEM (HR-TEM) images and selective area electron diffraction (SEAD) patterns were also obtained to examine the detailed microstructure of Co-Ti doped and Al doped SrM powder. As shown in Fig. 4, all HR-TEM images shows distinct lattice fringes. The calculated lattice distances of 0.25, 0.29, and 0.37 nm are indexed to the (114), (110), and (006) planes of M-type crystal structure, respectively [63, 64]. The SEAD patterns (insets in Fig. 4) of all SrM exhibited hexagonal symmetry, which is consistent with the hexagonal crystal structure of the SrM phase. In addition, the simple dot SAED patterns of the pure and doped SrM imply their single crystalline nature. Overall, these results suggest that all doped SrM powders exist as a single hexaferrite phase, which supports the previous XRD results.

3.2 Chemical State of Doped M-type Strontium Ferrites

To investigate changes in the chemical bonding or valence state of SrM induced by Co–Ti or Al doping, XPS was employed to analyze the binding energy of SrM. The
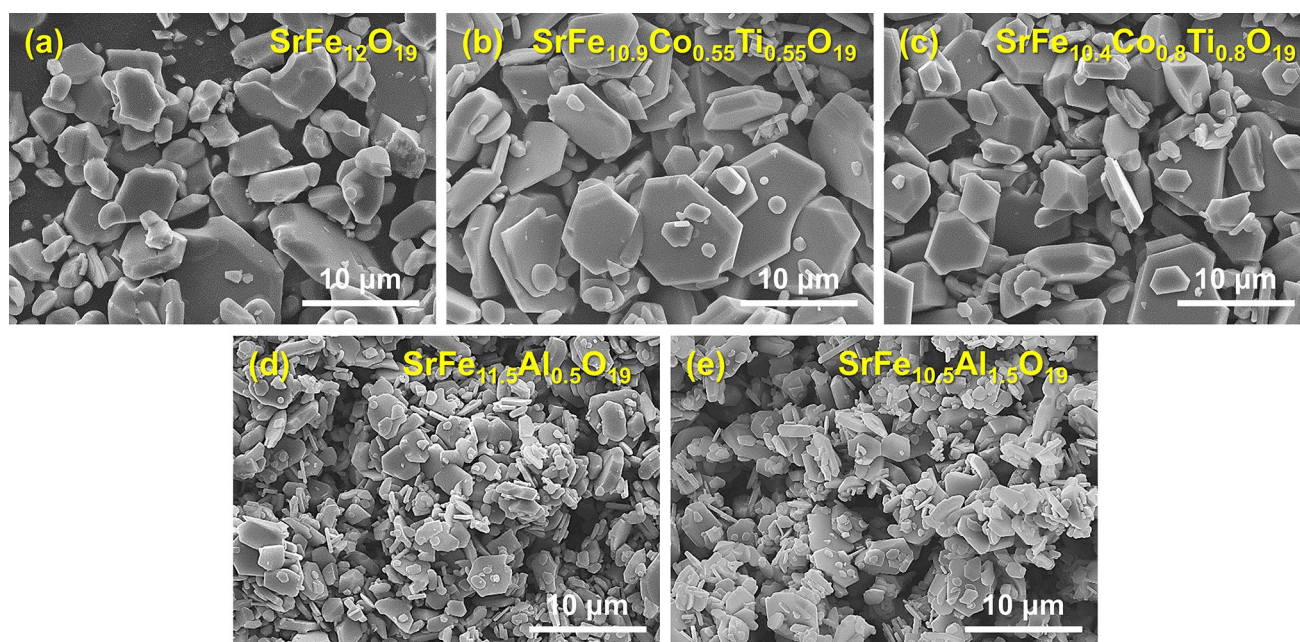

Fig. 3 SEM images of **a** pure SrM, **b, c** Co-Ti doped SrM, and **d, e** Al doped SrM powders
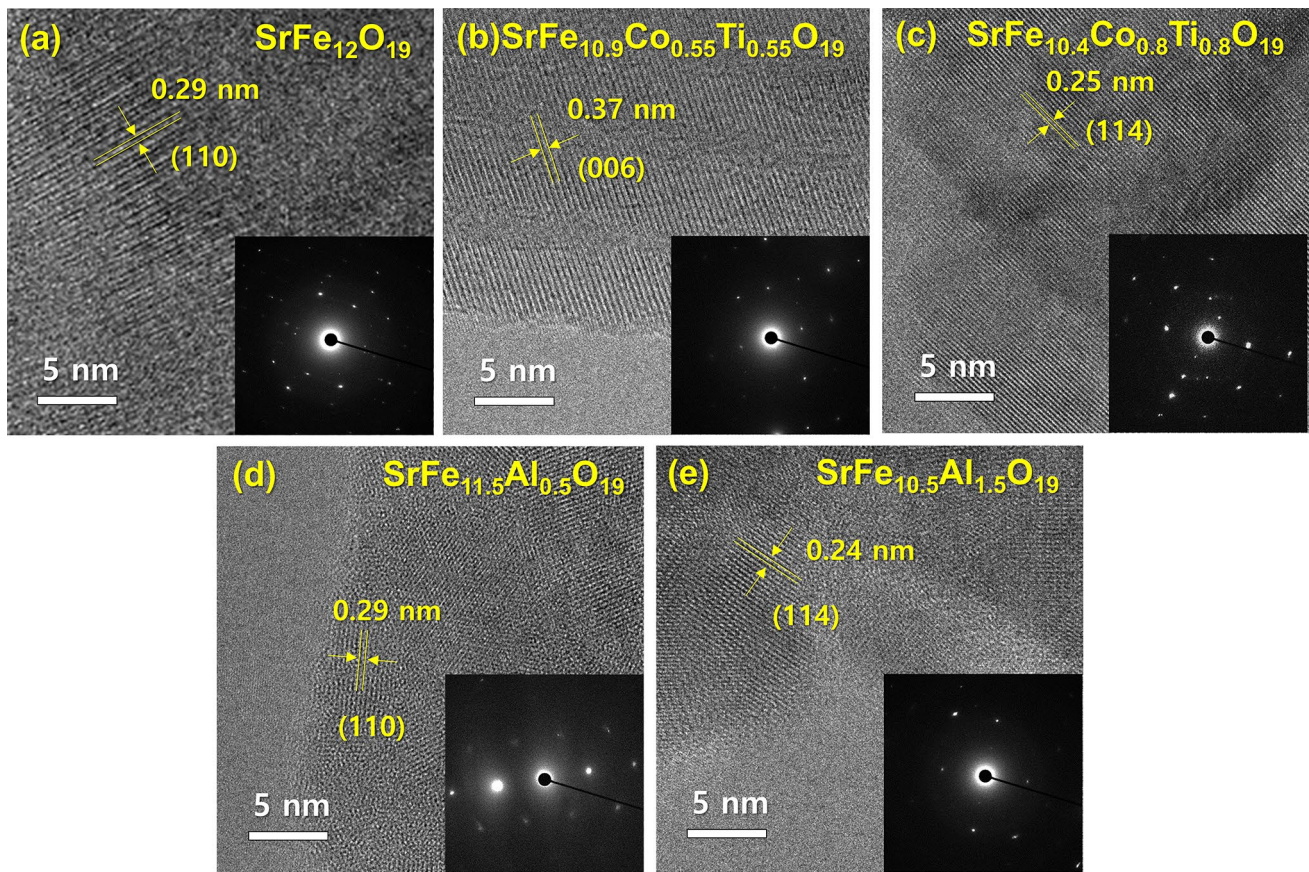
Fig. 4 HR-TEM images and SEAD patterns(inset) of **a** pure SrM, **b, c** Co-Ti doped SrM, and **d, e** Al doped SrM powders

high-resolution XPS spectra of pure, Co–Ti doped, and Al doped SrM are presented in Fig. 5. The spectra were calibrated using the standard binding energy of C $2s$ (284.6 eV), and were fitted with a mixture of Lorenzian and Gaussian functions, along with a Shirley background function.

The high-resolution Fe $2p$ spectrum of pure, Co–Ti, and Al doped SrM is presented in Fig. 5a-c. The spectra exhibit two main peaks at 711 and 724 eV, corresponding to Fe $2p_{3/2}$ and Fe $2p_{1/2}$, respectively. These peaks can be further deconvoluted into three peaks each, corresponding to Fe^{2+}, Fe^{3+}, and a satellite peak. Notably, the peak area of the Fe^{2+} ion in Co–Ti doped SrM is larger than that in pure or Al doped SrM, which is believed to be due to the higher Fe^{2+} ion content of Co–Ti doped SrM as a result of charge balance compensation by doping of Ti^{4+} ions with higher valence than three. Previous studies have also reported similar results for M-type ferrites doped with higher valence ions such as Zr^{4+} or Nb^{5+} [53, 55].

The XPS spectra of Fig. 5d, f shows Co $2p$ and Ti $2p$ spectra of Co-Ti doped SrM, and Al $2p$ spectra of Al doped SrM, respectively. The deconvolved peaks in all spectra are consistent with previously reported data [60, 65, 66]. The presence of trivalent Co^{3+} ions in Co-Ti doped SrM is attributed to the charge transfer between Fe^{3+} and Co^{2+} ions ($Fe^{3+} + Co^{2+} \leftrightarrow Fe^{2+} + Co^{3+}$). These XPS analysis results provide further evidence that Co–Ti and Al doped SrM have been successfully prepared.

3.3 Magnetic Properties of Doped M-type Strontium Ferrites

Figure 6a-b show the magnetic hysteresis loops of the Co-Ti doped and Al doped SrM powders at room temperature, respectively. Additionally, the detailed saturation magnetization (M_S) and coercive field (H_C) are presented in Table 2. Interestingly, pure and Co–Ti doped SrMs exhibited the
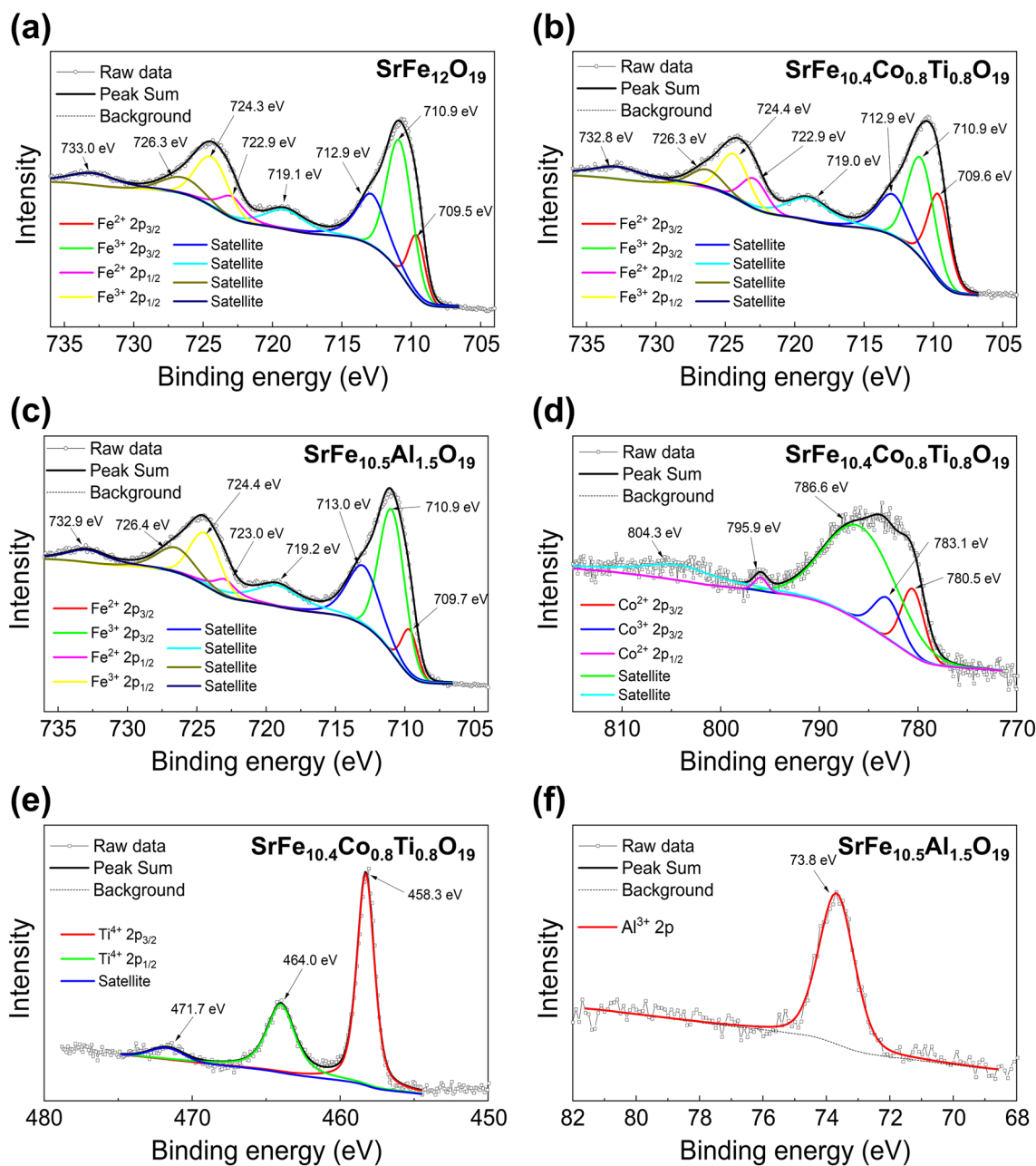
Fig. 5 High resolution XPS spectra of pure and doped SrM. **a** pure Fe 2*p* spectra, **b** Co-Ti doped Fe 2*p* spectra, **c** Al doped Fe-2*p* spectra, **d** Co-Ti doped Co 2*p* spectra, **e** Co-Ti doped Ti 2*p* spectra and **f** Al doped Al 2*p* spectra

typical hysteresis loop of single-phase magnetic materials, while the Al doped sample showed wasp-waisted hysteresis loops. This wasp waist hysteresis implies the presence of a small amount of secondary magnetic phase, but the existence of the secondary phase could not be confirmed by the XRD diffraction pattern in this study.

The value of M_S for pure SrM is 75.68 emu g^{-1}, which is similar to the theoretical value (~73 emu g^{-1}) [67]. As shown in Fig. 6 and Table 2, the M_S of CoTi doped SrM powder decreases slightly with increasing dopant concentrations. However, for Al doped SrM powder, a noticeable decrease in the M_S is observed with increasing doping concentrations. This different behavior of the M_S for doped SrM
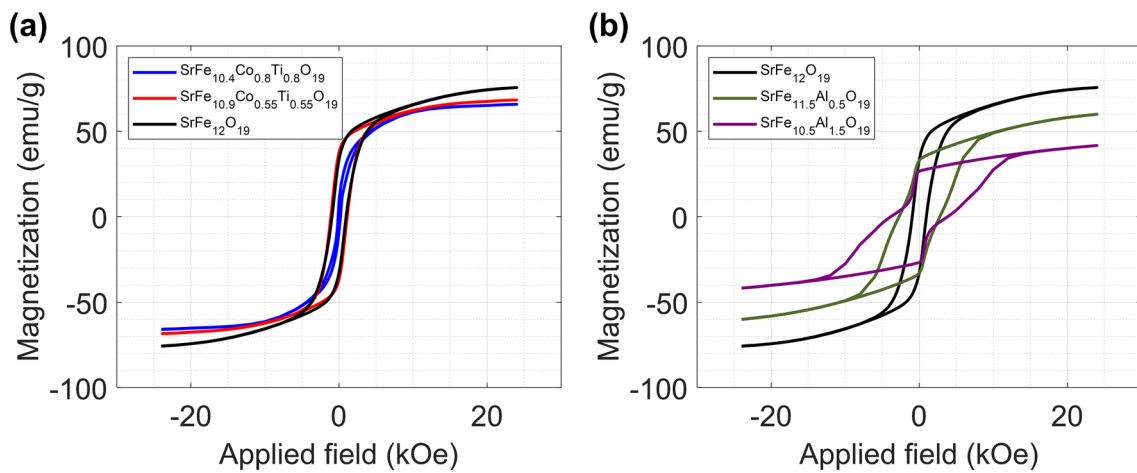
Fig. 6 Magnetic hysteresis loop of pure, **a** Co-Ti doped, and **b** Al doped SrM powders

Table 2 Saturation magnetization and coercive field of doped SrM powders

Composition	M_S (emu/g)	H_C (Oe)
$SrFe_{12}O_{19}$	75.68	952
$SrFe_{10.9}Co_{0.55}Ti_{0.55}O_{19}$	68.74	1104
$SrFe_{10.4}Co_{0.8}Ti_{0.8}O_{19}$	65.86	161
$SrFe_{11.5}Al_{0.5}O_{19}$	60.04	2757
$SrFe_{10.5}Al_{1.5}O_{19}$	41.72	3843

powder is associated with different preferential site occupancies for Co–Ti and Al ions. For M-type ferrite, Fe^{3+} ions occupy 5 different lattice sites, which are named 2a, 2b, 12 k, $4f^1$ and $4f^2$ (Fig. S1). 2a, 12 k and $4f^2$ are octahedral sites, $4f^1$ is a tetrahedral site and 2b is a trigonal bipyramidal site. The 2a, 2b and 12 k sites are spin-up, while $4f^1$ and $4f^2$ are spin down; thus, the total magnetization of M-type ferrite is contributed by the excess spin-up magnetic moment [67]. The magnetic moments of Fe^{3+}, Co^{2+}, Ti^{4+} and Al^{3+} are 5 μ_B, 3 μ_B, 0 μ_B, and 0 μ_B, respectively. Because Co^{2+}, Ti^{4+} and Al^{3+} ions show a lower magnetic moment than Fe^{3+} ions or zero magnetic moment, we can expect that the M_S will decrease if the dopant ions occupy spin-up sites such as 2a, 2b or 12 k and increase if the dopant ions occupy spin-down sites such as $4f^1$ and $4f^2$.

In previously reported Mössbauer spectra analysis, Co^{2+} and Ti^{4+} ions in co-doped M-type ferrites prefer to occupy $4f^2$ (spin down) and 2b (spin up), respectively [68–71]. Therefore, these opposite spin directions will cause a reduced dilution effect of the Co–Ti substitution for total

magnetization, and finally, the M_S of Co–Ti doped SrM slightly decreases with higher doping concentrations. However, according to the Mössbauer spectra analysis and first-principles total-energy calculations, Al^{3+} ions for M-type ferrites prefer to occupy 12 k (spin up) and 2a (spin up), respectively [72–74]. Therefore, the decrease in the M_S for Al doped SrM can be explained by substitution of non-magnetic ions for magnetic Fe^{3+} ions at the up-spin site, which reduced the total magnetization.

The coercive field (H_C) of doped SrM also showed different changing behaviors depending on the doping element and doping concentration. The H_C decreased as the doping concentration increased in Co–Ti doped SrM, resulting in soft magnetic properties; however, the H_C increased as the doping concentration increased in Al doped SrM, resulting in hard magnetic properties. This change in the coercive field can be explained by a difference in the particle size and a change in the magnetic anisotropy. The coercive field of a magnetic particle is generally related to the critical single domain size (D_C). According to previous studies, the critical single domain size of M-type ferrite is approximately 1 μm, and as the ferrite particle size increases or decreases, the coercive field decreases [59, 75]. As shown in Fig. 3, Co–Ti doped SrM powder mostly consists of hexagonal plate-shaped particles of 5 μm or larger, but Al doped SrM powder contains a large amount of particles with sizes of 1 μm. Therefore, it is considered that the H_C of Al doped SrM, whose particle size is similar to the critical single domain size, is greater than that of Co–Ti doped SrM.

The H_C of doped SrM is also changed by the magnetic anisotropy change due to the doping element and concentration.

M-type ferrite has a large c-axis anisotropy, and the magnitude of this anisotropy varies depending on the substitution site of the doped element. The decreased H_C of Co–Ti doped SrM is related to the spin rearrangement by Co^{2+} and Ti^{4+} ion substitutions. In particular, Co^{2+}–Ti^{4+} substituted at the 2b site reduces the uniaxial anisotropy so that the coercive field is greatly reduced according to the Co–Ti doping concentration [65, 76, 77]. The increased H_C of Al doped SrM is related to an enhancement of the magneto-crystalline anisotropy constant due to the substituted Al^{3+} ions at the 12 k site [58, 59, 78].

3.4 Electromagnetic Properties of the Doped M-type Strontium Ferrites

The incorporation of magnetic materials in EMI shielding materials provides various EMI absorption mechanisms including (1) hysteresis, (2) domain wall resonance, (3) eddy current, and (4) natural ferromagnetic resonance (FMR) [79]. In an oscillating magnetic field, the material magnetization is reversed, resulting in the dissipation of electromagnetic energy as heat. This dissipated energy is proportional to the area of the hysteresis loop. The oscillating magnetic field also induces a pressure that causes the domain walls in the magnetic material to oscillate. The oscillating domain wall dissipates its energy through the interaction with magnetic domains and the magnetic particle grain boundary [80]. Eddy current induced around a magnetic particle is dissipated as heat through Joule effect, as it is a current flowing through a conductor. However, these three mechanisms are known to be effective in low frequency range under several

GHz [81]. For microwave and mmWave applications, FMR is the most major contributor [82]. The resonance absorbs EMI and converts it into local heating of the material, resulting high magnetic loss tangent and imaginary permeability at the FMR frequency.

Figure 7 shows the complex permittivity (ε) and permeability (μ) of pure, Co–Ti doped and Al doped SrM composites. These composites consist of 70 wt% SrM and 30 wt% thermoplastic polyurethane (TPU). In each figure, the real parts and the imaginary parts are presented as solid lines and dashed lines, respectively. The real (ε') and imaginary (ε'') parts of the permittivity of all SrMs are not significantly different. As shown in Fig. 7b, all synthesized samples show clear FMR peaks of real (μ') and imaginary (μ'') permeability, but the FMR frequencies are different with the doping element and concentration. From Fig. 7b, it can be seen that the doping of Co–Ti shifts the FMR frequency to a lower frequency band, whereas Al doping pushes the FMR frequency to a higher frequency band. Furthermore, it was confirmed that the degree of the frequency shift increased with doping concentrations.

It is known that the FMR frequencies of the M-type ferrites are closely related to the magnetic anisotropy. The FMR frequency (f_r) is proportional to the anisotropy field (H_a) as:

$$f_r = \frac{\gamma}{2\pi}H_a = 1.4gH_a \tag{9}$$

where γ is the gyromagnetic ratio, and g is the Lande factor. Therefore, it can be expected that the substitution of Co-Ti decreases H_a, whereas the substitution of Al increases H_a. In fact, the contribution to the magnetic anisotropy of
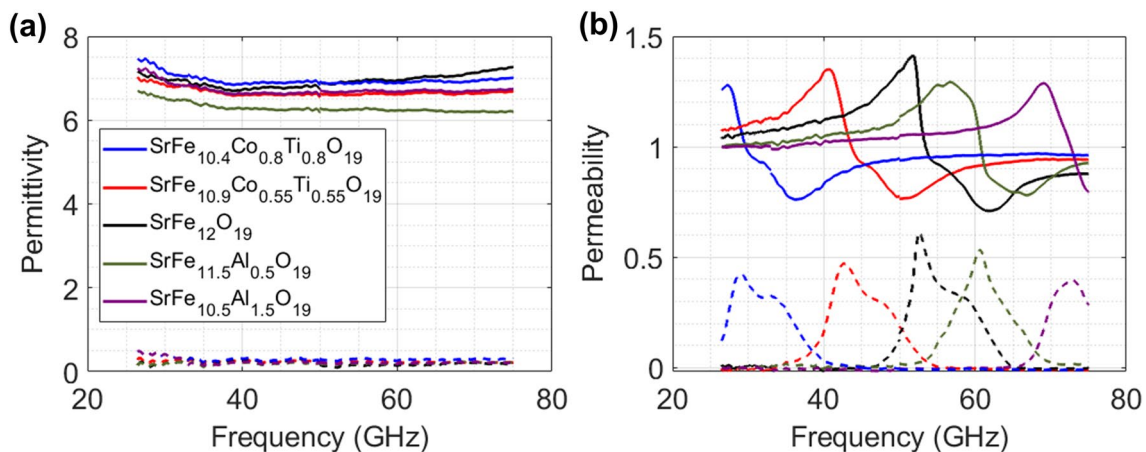

Fig. 7 **a** Permittivity and **b** permeability of pure, Co-Ti doped, and Al doped SrM composites

M-type hexaferrite differs at each Fe^{3+} site in the crystal lattice. According to previous reports, the replacement of Fe^{3+} ions at the 2b and 4f2 sites has the greatest contribution to the anisotropy field [83, 84]. The anisotropy field can be expressed by K_1 and M_S as:

$$H_a = \frac{2K_1}{M_S} \tag{10}$$

where K_1 is magnetocrystalline anistropy constant. The calculated K_1 for a single Fe^{3+} ion and the degree of contribution to H_a at each site are 1.4, 0.51, 0.23, 0.18, and -0.18 for the 2b, $4f^2$, 2a, $4f^1$, and 12 k sites, respectively [85]. In other words, when compared to other sites, the Fe^{3+} ions at the 2b site contribute the most to H_a, while the Fe^{3+} ions at the $4f^1$ and 12 k site contribute the least H_a.

As discussed above, the Co^{2+} and Ti^{4+} ions prefer to occupy 2b and $4f^2$, respectively. When Co–Ti is doped, Co^{2+} and Ti^{4+} ions replace Fe^{3+} ions in the 2b and $4f^2$ positions, which have high K_1 values. As a result, the K_1 value decreases significantly, but the Ms value decreases relatively less due to the opposite spin directions of the substituted site. Therefore, the H_a value of the Co–Ti doped SrM decreases, and the FMR frequency shifts to the low frequency band.

Unlike Co–Ti ions, Al^{3+} ions prefer to occupy 12 k and 2a sites. In particular, at high calcination temperatures, Al^{3+} ions are much more likely to occupy the 12 k site than the 2a site [74]. Since the K_1 value of a single Fe^{3+} at 12 k sites is negative, the total K_1 value of Al doped M-type ferrite will be increased. However, M_S is significantly decreased when nonmagnetic Al^{3+} ions are substituted for the up-spin 12 k and 2a sites. Therefore, the H_a value of Al doped SrM increases, and the FMR frequency shifts to a high frequency band.

Another factor affecting K_1 is the lattice parameters. It is known that the K_1 value of M-type ferrite is affected by the bond length between iron at the 2b (Fe_2) site and adjacent O atoms (O_3) [58]. As previously discussed, the lattice parameters of Al doped SrM were reduced due to the smaller ionic radius of Al^{3+} ions relative to Fe^{3+} ions. The crystal lattice contraction by Al^{3+} substitution decreases the bond length between Fe_2–O_3, which induces enlargement of the superexchange interaction. This increased superexchange interaction enhances the magnetic anisotropy, shifting the FMR frequencies to higher frequencies.

4 EMI Shielding Films with Multi-band Ultralow Reflection

4.1 EMI Shielding Film Design

Based on SrM, the EMI shielding film is proposed with a magnetic composite layer and a conductive grid (Fig. 8a, b). The composite layer is prepared by dispersing SrM powders to the TPU. Then, a 10 μm thick Cu grid is attached underneath the composite layer via hot pressing. This Cu grid is prepared through eletroforming to achieve a fine conductive grid with a 100 μm grid width and 100 μm gap between each grid (Fig. 8c). The cross-sectional SEM−EDS image in Fig. 8d shows that the composite layer with SrM (Yellow: Sr, Blue: Fe) and the Cu grid (Magenta) are bonded well to each other. According to ASTM D3359 Method B cross-cut adhesion test, the Cu grid has 4B/5B adhesion with the composite layer, which meets the standards of practical industrial applications (Fig. S2) [86]. Since the shielding film is submillimeter thin and TPU-based, the film is quite flexible and still intact even after folding and rolling (Fig. 8e, f).

The EMI shielding performance of a shielding material is composed of two parts: reflection and absorption. The EMI reflection from the shielding film can be explained with a transmission line model of electromagnetic waves (Fig. 8g). When the incident EMI faces the shielding film surface, the amount of reflected EMI, or reflection coefficient Γ, is defined as [87]:

$$\Gamma = \frac{Z_0 - Z_{in}}{Z_0 + Z_{in}} \tag{11}$$

where Z_0 is the electromagnetic impedance of air, and Z_{in} is the input impedance of the shielding film system. Therefore, it is important to minimize the impedance difference between the air and the shielding film to minimize the reflected amount of the EMI. As the shielding film consists of a composite layer and a grid, Z_{in} is given as [29, 88]:

$$Z_{in} = Z_c \frac{Z_L + Z_c \tanh \gamma d}{Z_c + Z_L \tanh \gamma d} \tag{12}$$

$$Z_c = Z_0 \sqrt{\frac{\mu}{\varepsilon}} \tag{13}$$

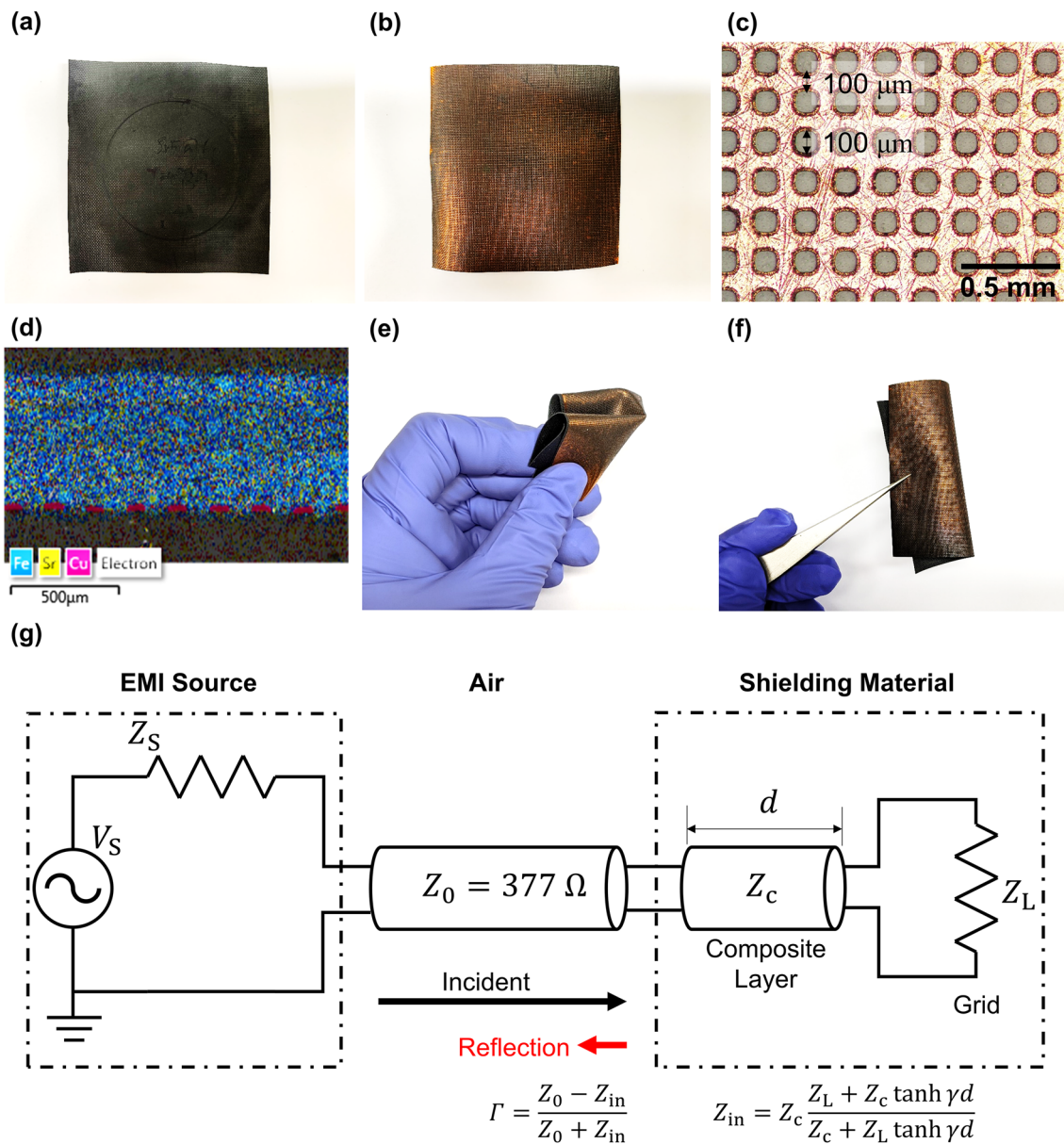$$\gamma = j2\pi f \frac{\sqrt{\mu\varepsilon}}{c} \tag{14}$$

Fig. 8 The proposed EMI shielding film design: **a, b** Front and back view of the film. **c** Optical microscopic image of the Cu grid. **d** SEM–EDS cross section image of the film. **e, f** Folded and rolled shielding films. **g** Transmission line model of the proposed shielding film

where Z_c is the electromagnetic impedance of the composite layer; Z_L is the electromagnetic impedance of the conductive grid; d is the thickness of the composite layer; μ and ε are the complex permeability and permittivity of the composite layer, respectively; f is the EMI frequency; j is the imaginary unit; γ is the electromagnetic wave propagation constant and c is the speed of light in free space.

From the above equations, given μ, ε, d, and Z_L, a single local minimum of Γ exists at a specific frequency if μ and ε are frequency independent. However, if there is a sudden

increase in μ and ε, as proposed with FMR frequency tunable SrMs (Fig. 7), an additional impedance matching occurs at the FMR frequency, and additional local minimum appears close to the FMR frequency (Fig. S3). This enables ultralow reflection at multiple frequencies and low reflection in a wider frequency band. It should be noted that the Γ depends on not only permeability of the composite layer but also its permittivity. To adjust the real and imaginary permittivity for optimized Γ, dielectric filler materials, e.g.,

silver nanowire [89], graphene [90], or carbon black [91], can be included to the composite layer. Carbon nanotubes are one of the most favorable dielectric filler thanks to their lightweight nature and high permittivity change with a small amount of their incluson.

Therefore, by carefully tailoring the composite layer characteristics and grid characteristics, including the FMR frequency of SrMs in the composite layer, it is possible to have ultralow reflection at the desired two frequency bands: one corresponding to the FMR frequency and the other corresponding to the film composition. Additionally, the grid impedance can be controlled by changing the grid width and gap. As the conductive area increases, with a wider grid and narrower gap between them, the grid becomes similar to a conductive metal layer, and its impedance decreases to zero. On the other hand, with a narrower grid and wider gap, a smaller portion of the conductive material increases the Z_L. It has been investigated that a proper selection of Z_L helps decrease the reflection of a grid-based shielding film [29]. Then, the SER is given as:

$$\text{SER} = -10\log\left(1 - |S_{11}|^2\right) = -10\log(1 - |\Gamma|^2) \quad (15)$$

where S_{11} is a scattering parameter corresponding to EMI reflection. For more details regarding Eq. (15), the experimental section can be referenced.

The other part of EMI shielding, absorption, can be explained as electromagnetic wave attenuation in a lossy material. Due to the dielectric and magnetic loss of the material, the electromagnetic wave amplitude decays exponentially as it passes through the material [92]. Then, the absorption shielding effectctiveness (SEA) of the material is defined as [4]:

$$\text{SEA} = -10\log_{10}\left(\frac{|S_{21}|^2}{1 - |S_{11}|^2}\right) = 20\log_{10}|e^{\gamma t}| = 20\alpha t\log_{10}e \quad (16)$$

where α is the attenuation constant of the electromagnetic waves in the material, and t is the material thickness. For a non-conducting material, e.g., the composite layer of the proposed shielding film, the attenuation constant is given as [38]:

$$\alpha = \text{Re}(\gamma)$$

$$= \frac{\pi f}{c}\sqrt{2\mu'\varepsilon'}\sqrt{\frac{\mu''\varepsilon''}{\mu'\varepsilon'} - 1 + \sqrt{\left(\frac{\mu''}{\mu'}\right)^2 + \left(\frac{\varepsilon''}{\varepsilon'}\right)^2 + \left(\frac{\mu''\varepsilon''}{\mu'\varepsilon'}\right)^2 + 1}} \quad (17)$$

From Eqs. (16) and (17), it is shown that the SEA increases with (1) thicker material or (2) higher dielectric/magnetic loss. The major energy transformation mechanism of dielectric lossy fillers, CNT in the proposed shielidng film, is Joule effect [93]. A given external electric field, the electromagnetic waves, displaces charges in the dielectric filler and causes dielectric polarization. This enables the dielectric filler to store electric potential energy. As this system can be considered as a circuit with a capacitor (the real part of permittivity) and a resistance (the imaginary part of permittivity), the stored electromagnetic energy is transformed and dissipated as heat at the resistance. On the other hand, the magnetic lossy fillers absorb electromagnetic waves by (1) hysteresis, (2) domain wall resonance, (3) eddy current, and (4) natural ferromagnetic resonance (FMR), and FMR is the most major contributor in mmWave applications. Therefore, it is important to increase the electromagnetic loss, especially with FMR in this study, to have a high SEA with less thickness. The synergetic effects between magnetic loss from ferromagnetic resonance of SrMs and dielectric loss from CNT as well as interfacial polarization in the composite layer are favorable for enhancement of EMI absorption capabilities [42]. These equations also show why foam materials need to be thicker, as they are electromagnetically less lossy with a high void content.

For a multilayer structure such as the proposed shielding film, the total SEA is known to be the sum of the SEAs of each layer. For a conducting material, e.g., the conductive grid of the proposed shielding film, the attenuation constant is

$$\alpha = \sqrt{\pi f \mu \sigma} \quad (18)$$

where σ is the electric conductivity. As the conductive grid shows more than 30 dB SEA thanks to its high conductivity, the total SE of the proposed shielidng film becomes higher with the conductive grid and high magnetic loss of the composite layer.

4.2 5G Telecommunication Application: 39/52 GHz Shielding Film

Based on the aforementioned design factors, two types of mmWave EMI shielding films with ultralow reflection are designed. The first film focuses on shielding 39 and 52 GHz frequency bands, which corresponds to future 5G wireless communication band candidates [94]. In particular, the
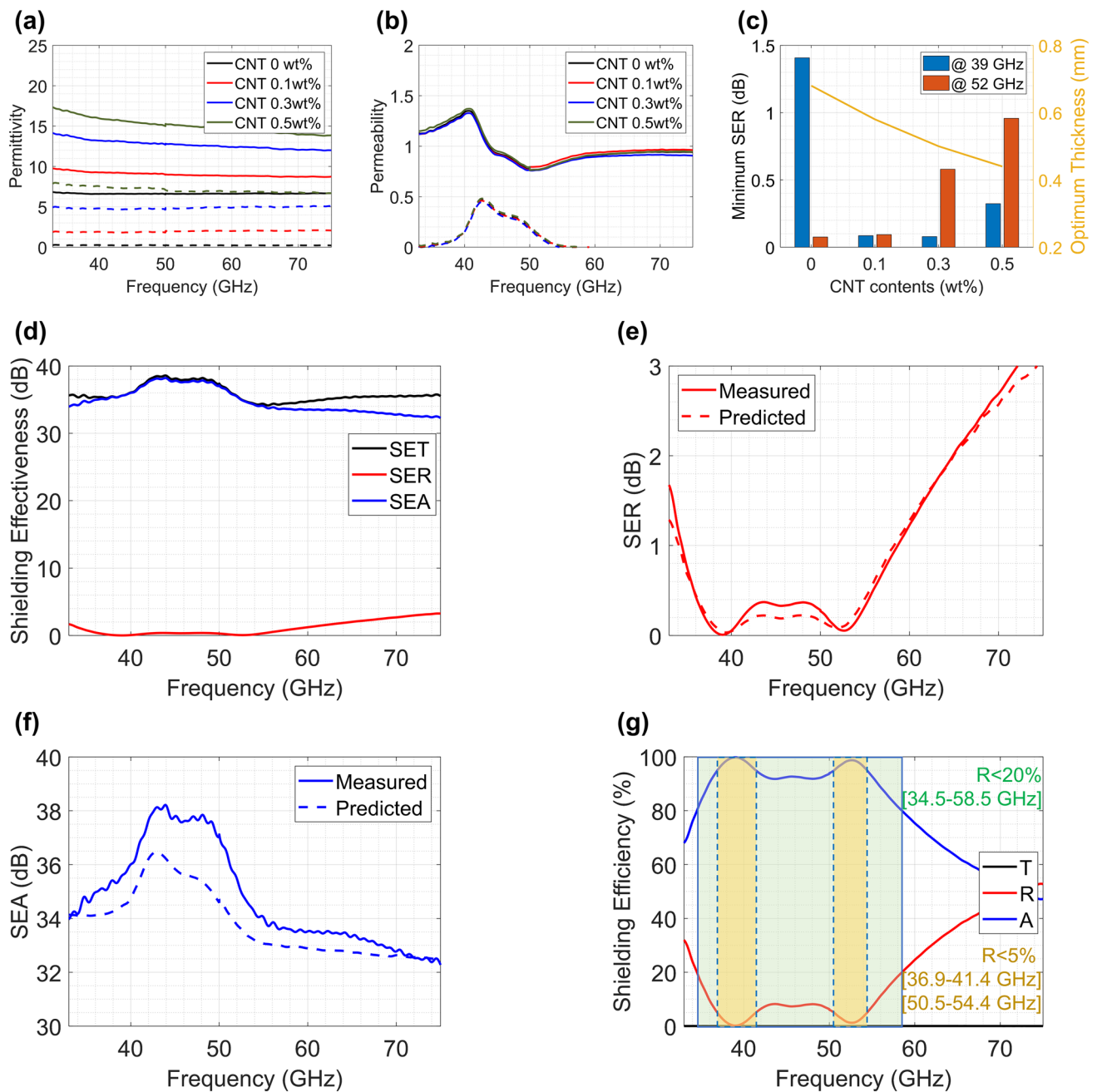
Fig. 9 EMI shielding film for 5G telecommunication applications: **a** Complex permittivity and **b** permeability of composite layers with different CNT contents. **c** Estimated minimum SER of each specimen at 39 and 50 GHz. **d** Measured shielding effectiveness of the prepared EMI shielding film. Comparison of the measured and predicted **e** SER and **f** SEA. **g** The measured shielding efficiency of the prepared EMI shielding film

39 GHz band (37–40 GHz) is known as the 5G Band n260, and most major carriers in the US, including AT&T and Verizon, already acquired this band through a frequency band auction by the Federal Communication Commission [95]. The composite layer of this film includes 70 wt%

$SrFe_{10.9}Co_{0.55}Ti_{0.55}O_{19}$ which is SrM with an FMR frequency near 39 GHz. The layer contains CNTs as well to control its permittivity to optimize the input impedance of Eq. (12). Figure 9a–b presents the measured complex permittivity and permeability of the composite layer with different amounts

of CNTs. Both the real (solid lines in Fig. 9a) and imaginary (dashed lines in Fig. 9a) permittivity increase with additional CNT content, while the permeability does not change as CNTs are not magnetic materials. The SER of shielding films with each composite layer can be estimated using the proposed transmission line model and Eq. (15). Figure 9c presents the calculated minimum SER at 39 and 52 GHz with different CNT contents at the optimum layer thickness. It has been shown that the shielding film may have the lowest SER with 0.1 wt% CNTs and a 0.58 mm layer thickness.

Based on this estimation, the actual shielding film is fabricated, and its EMI shielding performance is evaluated. Figure 9d presents the measured SE at 33–75 GHz, and Fig. 9e and f provide closer looks of the SER and SEA, respectively. This film shows an exceptionally low SER of less than 0.1 dB at 39 and 52 GHz, while shielding more than 30 dB over the entire frequency range. The first minimum SER frequency (0.009 dB at 38.9 GHz) is located around the FMR frequency of the doped SrM, and the other minimum SER frequency (0.055 dB at 52.5 GHz) is determined with the layer composition. The SEA shows a high peak in the 40–50 GHz band due to the high magnetic loss around the FMR frequency. It should also be noted that the predicted SER and SEA using the theoretical model (Eqs. 15, 16), presented as dashed lines in Fig. 9e–f, match very well with the measured values (solid lines).

The outstanding shielding performance of the film is better presented with its high shielding efficiency (Fig. 9g). The film reflects only 0.2% and absorbs 99.7% of EMI at 39 GHz and reflects only 1.6% and absorbs 98.3% at 52 GHz. Moreover, not only at these specific frequencies, the film shows ultralow reflection of less than 5% in two bands, including each frequency (36.9–41.4 GHz and 50.5–54.4 GHz), and low reflection less than 20% in a broad frequency band (34.5–58.5 GHz). It should be noted that the first ultralow reflection band covers the whole n260 band (37–40 GHz). This implies that the proposed shielding film can solve EMI problems in 39 and 52 GHz telecommunication bands.

4.3 Automotive Radar Application: 60/77 GHz Shielding Film

The other film focuses on shielding 60 and 77 GHz frequency bands, which correspond to automotive radar bands. There is an increasing usage of radars for automobiles, and

77 GHz long range radar is essential for recently manufactured autonomous vehicles with ADAS [96]. 60 GHz radar is also of interest for multi-functional in-cabin monitoring systems, e.g., child presence detection, gesture detection, and driver vital monitoring [97]. The composite layer of this film contains 70 wt% $SrFe_{11.5}Al_{0.5}O_{19}$ and SrM with an FMR frequency near 60 GHz. The layer also contains CNTs to control its permittivity. Figure 10a and b present the measured complex permittivity and permeability of the composite layer with different amounts of CNTs, respectively. According to the proposed transmission line model, the shielding film may have the lowest SER with 0.1 wt% CNTs and a 0.34 mm layer thickness (Fig. 10c).

Figure 10d presents the measured SE of the fabricated shielding film on 33–110 GHz with closer looks of the SER (Fig. 10e) and SEA (Fig. 10f). As in the previous example, the first minimum SER frequency (0.065 dB at 59.3 GHz) is located around the FMR frequency, and the other minimum SER frequency (0.12 dB at 74.8 GHz) is determined with the layer composition. The predicted SER and SEA also match very well with the measured values.

The efficiency is also presented in Fig. 10g. The film reflects only 1.5 and absorbs 98.4% of EMI at 60 GHz; moreover, it reflects only 2.9% and absorbs 97.0% at 77 GHz. In addition to these specific frequencies, the film shows ultralow reflection of less than 5% in two bands (56.3–60.8 GHz and 72.7–80.4 GHz) and low reflection less than 20% in a broad frequency band (53.8–91.8 GHz). This shows that the proposed shielding film can work as an effective EMI shielding film for a wide mmWave frequency range including 60 and 77 GHz automotive radar bands.

4.4 Comparison with Previous Studies

Two examples of mmWave EMI shielding films with ultralow reflection are presented, one for 39/52 GHz 5G telecommunication and the other for 60/77 GHz automotive radars. The EMI shielding performance of these films is compared with previously reported shielding materials for mmWave frequencies, including 26 [5, 6, 8–10, 18, 25–31, 98–100], 39 [2, 6, 7, 13, 18, 25, 31–34, 101–106], and 77 GHz [107, 108] (the exact values are presented in Table S1). In Fig. 11a, conductive shielding materials are located on the bottom-right side, indicating that they are reflection-dominant materials that
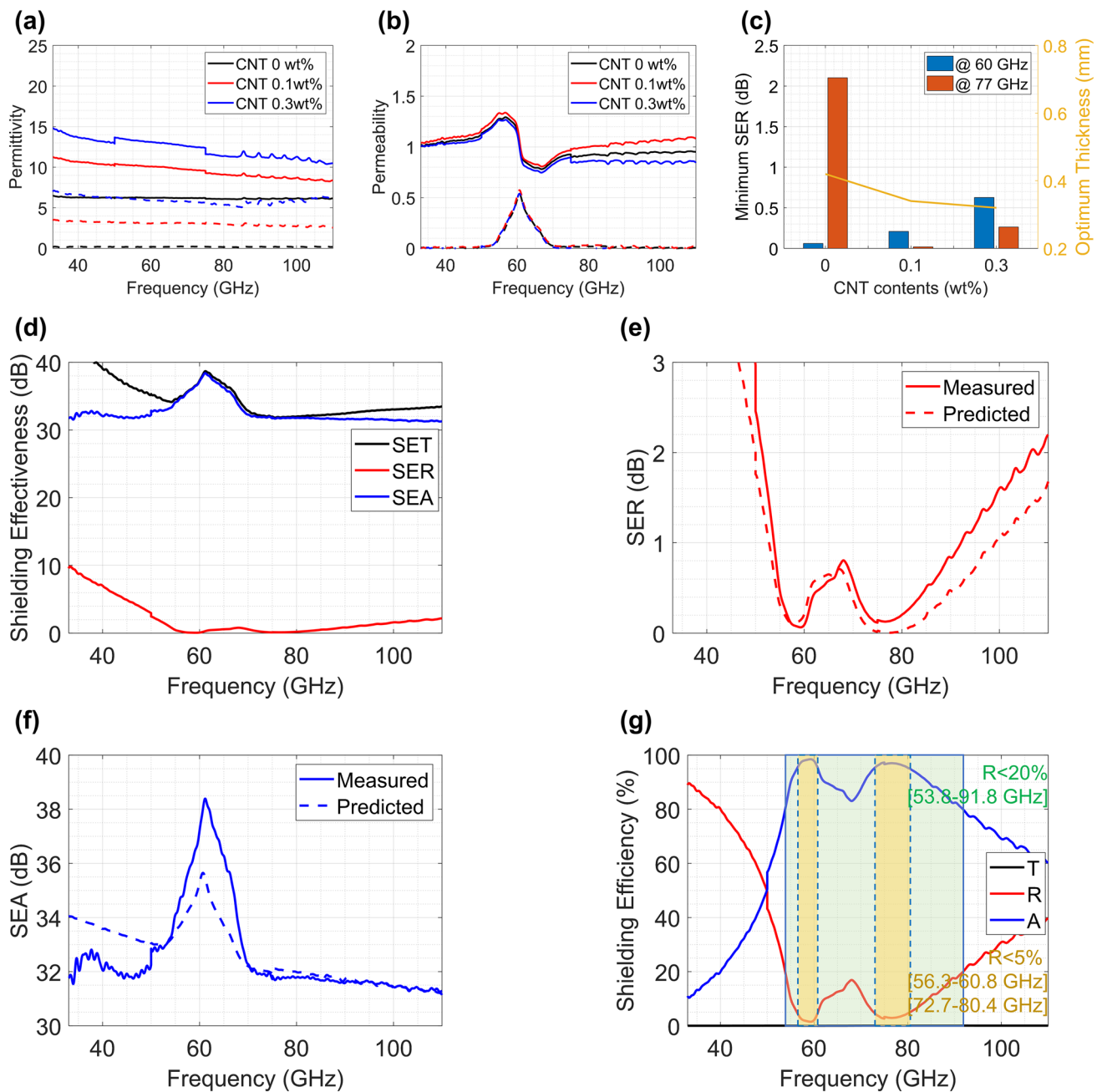
Fig. 10 EMI shielding film for automotive radar applications: **a** Complex permittivity and **b** permeability of composite layers with different CNT contents. **c** Estimated minimum SER of each specimen at 60 and 77 GHz. **d** Measured shielding effectiveness of the prepared EMI shielding film. Comparison of the measured and predicted **e** SER and **f** SEA. **g** The measured shielding efficiency of the prepared EMI shielding film

reflect more than 80% of the incident EMI. Magnetic and dielectric composite materials are more absorption-dominant, but their reflectance is still more than 20%. Foam-type shielding materials also show less reflectance, but their thicknesses are usually more than several millimeters, and their applications in mobile devices are limited. On the other hand, composite shielding materials with conductive grids, including the proposed works, outperform other reports with exceptionally ultralow reflectance < 5%.
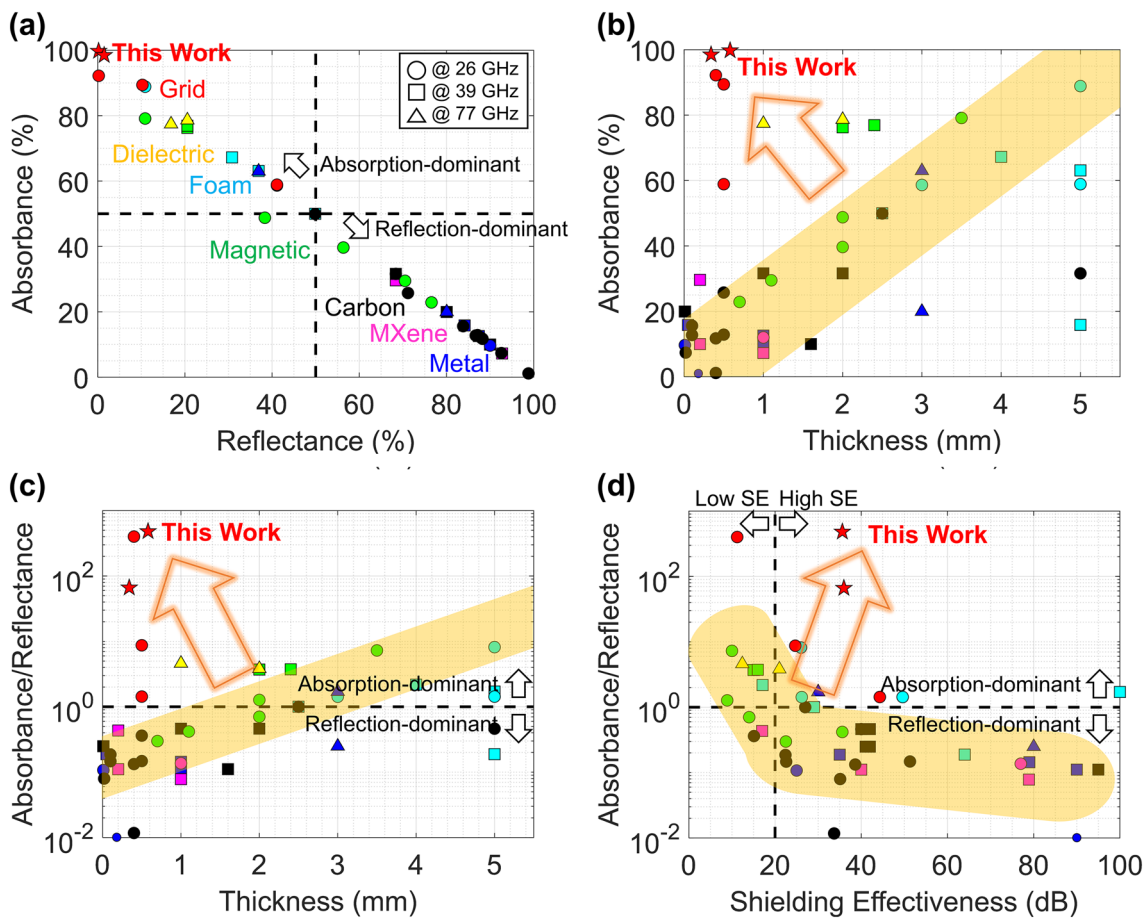
Fig. 11 Comparison of the EMI shielding performance of the proposed works (red stars) with previous literature. **a** Reflectance vs. absorbance. **b** Thickness vs. absorbance. **c** Thickness vs. absorbance/reflectance ratio. **d** Shielding effectiveness vs. absorbance/reflectance ratio

This is better represented in Fig. 11b–c with thickness comparison. Most shielding materials tend to be thicker to be more absorption-dominant (high absorbance and high absorbance/reflectance ratio (ARR)), as presented with yellow regions in the figures. The proposed shielding films absorb more than 95% of the incident EMI with sub-millimeter thicknesses using FMR tunable doped SrMs for mmWave frequencies and tailored conductive grid design. This helps reduce EMI reflection and minimize its secondary pollution, which is necessary for mmWave applications.

In addition, it should be noted that the proposed films show not only high absorbance but also high SE. Figure 11d shows that shielding materials with high SE tend to be reflection-dominant, while absorption-dominant materials show low SE. As many 5G applications require severe EMI shielding standards higher than 20 dB SE [109, 110], it is

important to simultaneously achieve minimized reflectance and maximized SE. To the best of the authors' knowledge, the proposed films are the only materials performing more than 30 dB SE and 60 ARR, which correspond to more than 99.9% EMI shielding and 98% absorption, and less than 2% EMI reflection. As doped SrM powders in the composite layer effectively absorb electromagnetic energy with its high magnetic loss, it is possible to achieve a high SE while still being absorption dominant.

5 Conclusions

In this study, EMI shielding films with multi-band ultralow reflection are proposed. By combining a magnetic composite layer and a conductive grid, an absorption-dominant shielding material with high SE is achieved with sub-millimeter

thicknesses. By tuning the (1) FMR frequency of SrM powders in the magnetic composite layer and (2) composite layer geometries, the frequency bands with ultralow reflections can be controlled. Two examples are presented in this study. The first 0.58 mm film shields 34.5–58.5 GHz frequency band using Co-Ti doped SrM powders with an FMR near 39 GHz, which minimizes EMI reflection at 39 and 52 GHz 5G telecommunication frequencies. The other 0.34 mm film shields 53.8–91.8 GHz frequency band using Al doped SrM powders with FMR near 60 GHz, which minimizes EMI reflection at 60 and 77 GHz automotive radar frequencies.

The EMI shielding performance of the proposed films is compared with those of previous literature, which shows that the proposed films outperform other shielding materials with their high absorbance, low reflectance, high SE and sub-millimeter thicknesses. This is necessary for 5G EMI shielding materials to avoid secondary EMI pollution with tight component-to-component spacing in integrated mobile modules. Additional studies are underway to (1) enhance the SE of the films using doped M-type ferrites with higher magnetic loss and (2) achieve additional ultralow reflection bands using complex grid patterns and layer compositions.

References

1. G.-M. Weng, J. Li, M. Alhabeb, C. Karpovich, H. Wang et al., Layer-by-layer assembly of cross-functional semi-transparent mxene-carbon nanotubes composite films for next-generation electromagnetic interference shielding. Adv. Funct. Mater. **28**(44), 1803360 (2018). https://doi.org/10.1002/adfm.201803360

2. B. Yao, W. Hong, T. Chen, Z. Han, X. Xu et al., Highly stretchable polymer composite with strain-enhanced electromagnetic interference shielding effectiveness. Adv. Mater. **32**(14), 1907499 (2020). https://doi.org/10.1002/adma.201907499

3. D. Ammen, M. Umehira, X. Wang, S. Takeda, H. Kuroda, in A ghost target suppression technique using interference replica for automotive fmcw radars. 2020 IEEE Radar Conference (RadarConf20). 1-5 (2020). https://doi.org/10.1109/RadarConf2043947.2020.9266514

4. M. Peng, F. Qin, Clarification of basic concepts for electromagnetic interference shielding effectiveness. J. Appl. Phys. **130**(22), 225108 (2021). https://doi.org/10.1063/5.0075019

5. N. Zhang, R. Zhao, D. He, Y. Ma, J. Qiu et al., Lightweight and flexible ni-co alloy nanoparticle-coated electrospun polymer nanofiber hybrid membranes for high-performance electromagnetic interference shielding. J. Alloys Compd. **784**, 244–255 (2019). https://doi.org/10.1016/j.jallcom.2018.12.341

6. H. Wang, C. Ji, C. Zhang, Y. Zhang, Z. Zhang et al., Highly transparent and broadband electromagnetic interference shielding based on ultrathin doped ag and conducting oxides hybrid film structures. ACS Appl. Mater. Interfaces **11**(12), 11782–11791 (2019). https://doi.org/10.1021/acsami.9b00716

7. Y. Xu, Z. Lin, K. Rajavel, T. Zhao, P. Zhu et al., Tailorable, lightweight and superelastic liquid metal monoliths for multifunctional electromagnetic interference shielding. Nano-Micro Lett. **14**(1), 29 (2021). https://doi.org/10.1007/s40820-021-00766-5

8. S. Zeng, X. Li, M. Li, J. Zheng et al., Flexible pvdf/cnts/ni@cnts composite films possessing excellent electromagnetic interference shielding and mechanical properties under heat treatment. Carbon **155**, 34–43 (2019). https://doi.org/10.1016/j.carbon.2019.08.024

9. B. Zhao, C. Zhao, R. Li, S.M. Hamidinejad, C.B. Park, Flexible, ultrathin, and high-efficiency electromagnetic shielding properties of poly(vinylidene fluoride)/carbon composite films. ACS Appl. Mater. Interfaces **9**(24), 20873–20884 (2017). https://doi.org/10.1021/acsami.7b04935

10. B. Zhao, S. Wang, C. Zhao, R. Li, S.M. Hamidinejad et al., Synergism between carbon materials and ni chains in flexible poly (vinylidene fluoride) composite films with high heat dissipation to improve electromagnetic shielding properties. Carbon **127**, 469–478 (2018). https://doi.org/10.1016/j.carbon.2017.11.032

11. Z. Zeng, G. Wang, B.F. Wolan, N. Wu, C. Wang et al., Printable aligned single-walled carbon nanotube film with outstanding thermal conductivity and electromagnetic interference shielding performance. Nano-Micro Lett. **14**(1), 179 (2022). https://doi.org/10.1007/s40820-022-00883-9

12. R. Yang, X. Gui, L. Yao, Q. Hu, L. Yang et al., Ultrathin, lightweight, and flexible cnt buckypaper enhanced using mxenes for electromagnetic interference shielding. Nano-Micro Lett. **13**(1), 66 (2021). https://doi.org/10.1007/s40820-021-00597-4

13. H. Jia, X. Yang, Q.-Q. Kong, L.-J. Xie, Q.-G. Guo et al., Free-standing, anti-corrosion, super flexible graphene oxide/silver nanowire thin films for ultra-wideband electromagnetic interference shielding. J. Mater. Chem. A **9**(2), 1180–1191 (2021). https://doi.org/10.1039/D0TA09246K

14. P. Song, B. Liu, C. Liang, K. Ruan, H. Qiu et al., Lightweight, flexible cellulose-derived carbon aerogel@reduced graphene oxide/pdms composites with outstanding emi shielding performances and excellent thermal conductivities. Nano-Micro Lett. **13**(1), 91 (2021). https://doi.org/10.1007/s40820-021-00624-4

15. P. Song, Z. Ma, H. Qiu, Y. Ru, J. Gu, High-efficiency electromagnetic interference shielding of rgo@feni/epoxy composites with regular honeycomb structures. Nano-Micro Lett. **14**(1), 51 (2022). https://doi.org/10.1007/s40820-022-00798-5

16. J. Liu, H.-B. Zhang, R. Sun, Y. Liu, Z. Liu et al., Hydrophobic, flexible, and lightweight mxene foams for high-performance electromagnetic-interference shielding. Adv. Mater. **29**(38), 1702367 (2017). https://doi.org/10.1002/adma.201702367

17. G. Yin, Y. Wang, W. Wang, Z. Qu, D. Yu, A flexible electromagnetic interference shielding fabric prepared by construction of PaNi/mxene conductive network via layer-by-layer assembly. Adv. Mater. Interfaces **8**(6), 2001893 (2021). https://doi.org/10.1002/admi.202001893

18. V.-T. Nguyen, B.K. Min, Y. Yi, S.J. Kim, C.-G. Choi, Mxene ($Ti_3C_2T_x$)/graphene/pdms composites for multifunctional broadband electromagnetic interference shielding skins. Chem. Eng. J. **393**, 124608 (2020). https://doi.org/10.1016/j.cej.2020.124608

19. L.X. Liu, W. Chen, H.B. Zhang, L. Ye, Z. Wang et al., Super tough and environmentally stable aramid. Nanofiber@mxene coaxial fibers with outstanding electromagnetic interference shielding efficiency. Nano-Micro Lett. **14**(1), 111 (2022). https://doi.org/10.1007/s40820-022-00853-1

20. P. Dixon, in Emi mitigation at millimeter wave. 2019 European Microwave Conference in Central Europe (EuMCE). (2019), pp. 610-613

21. J.-H. Lee, Y.-S. Kim, H.-J. Ru, S.-Y. Lee, S.-J. Park, Highly flexible fabrics/epoxy composites with hybrid carbon nanofillers for absorption-dominated electromagnetic interference shielding. Nano-Micro Lett. **14**(1), 188 (2022). https://doi.org/10.1007/s40820-022-00926-1

22. L. Zou, C. Lan, S. Zhang, X. Zheng, Z. Xu et al., Near-instantaneously self-healing coating toward stable and durable electromagnetic interference shielding. Nano-Micro Lett. **13**(1), 190 (2021). https://doi.org/10.1007/s40820-021-00709-0

23. M. Zhang, C. Han, W.-Q. Cao, M.-S. Cao, H.-J. Yang et al., A nano-micro engineering nanofiber for electromagnetic absorber, green shielding and sensor. Nano-Micro Lett. **13**(1), 27 (2020). https://doi.org/10.1007/s40820-020-00552-9

24. X. Jia, Y. Li, B. Shen, W. Zheng, Evaluation, fabrication and dynamic performance regulation of green emi-shielding materials with low reflectivity: a review. Compos. B Eng. **233**, 109652 (2022). https://doi.org/10.1016/j.compositesb.2022.109652

25. B. Zhao, C. Zhao, M. Hamidinejad, C. Wang, R. Li et al., Incorporating a microcellular structure into PVDF/graphene–nanoplatelet composites to tune their electrical conductivity and electromagnetic interference shielding properties. J. Mater. Chem. C **6**(38), 10292–10300 (2018). https://doi.org/10.1039/C8TC03714K

26. K. Pubby, S.B. Narang, Ka band absorption properties of substituted nickel spinel ferrites: Comparison of open-circuit approach and short-circuit approach. Ceram. Int. **45**(17), 23673–23680 (2019). https://doi.org/10.1016/j.ceramint.2019.08.081

27. O. Pitkänen, J. Tolvanen, I. Szenti, Á. Kukovecz, J. Hannu et al., Lightweight hierarchical carbon nanocomposites with highly efficient and tunable electromagnetic interference shielding properties. ACS Appl. Mater. Interfaces **11**(21), 19331–19338 (2019). https://doi.org/10.1021/acsami.9b02309

28. Z. Bai, B. Zhao, J. Deng, Y. Ren, Y. Li et al., Light-weight and high-efficiency electromagnetic wave shielding properties based on waste straw porous carbon. J. Mater. Sci. Mater. Electron. **31**(6), 4963–4971 (2020). https://doi.org/10.1007/s10854-020-03063-w

29. S.H. Ryu, Y.K. Han, S.J. Kwon, T. Kim, B.M. Jung et al., Absorption-dominant, low reflection emi shielding materials with integrated metal mesh/tpu/cip composite. Chem. Eng. J. **428**, 131167 (2022). https://doi.org/10.1016/j.cej.2021.131167

30. S.H. Ryu, B. Park, Y.K. Han, S.J. Kwon, T. Kim et al., Electromagnetic wave shielding flexible films with near-zero reflection in the 5g frequency band. J. Mater. Chem. A **10**(8), 4446–4455 (2022). https://doi.org/10.1039/D1TA10065C

31. Y. Zhang, B. Zhang, K. Li, G.-L. Zhao, S.M. Guo, Electromagnetic interference shielding effectiveness of high entropy alcocrfeni alloy powder laden composites. J. Alloys Compd. **734**, 220–228 (2018). https://doi.org/10.1016/j.jallcom.2017.11.044

32. Y. Jia, T.D. Ajayi, B.H. Wahls, K.R. Ramakrishnan, S. Ekkad et al., Multifunctional ceramic composite system for simultaneous thermal protection and electromagnetic interference shielding for carbon fiber-reinforced polymer composites. ACS Appl. Mater. Interfaces **12**(52), 58005–58017 (2020). https://doi.org/10.1021/acsami.0c17361

33. J. Wei, Z. Lin, Z. Lei, Y. Xu, Z. Zhao et al., Lightweight and highly compressible expandable polymer microsphere/silver nanowire composites for wideband electromagnetic interference shielding. ACS Appl. Mater. Interfaces **14**(4), 5940–5950 (2022). https://doi.org/10.1021/acsami.1c20593

34. B. Zhao, R. Wang, Y. Li, Y. Ren, X. Li et al., Dependence of electromagnetic interference shielding ability of conductive polymer composite foams with hydrophobic properties on cellular structure. J. Mater. Chem. C **8**(22), 7401–7410 (2020). https://doi.org/10.1039/D0TC00987C

35. L. Ma, M. Hamidinejad, B. Zhao, C. Liang, C.B. Park, Layered foam/film polymer nanocomposites with highly efficient emi shielding properties and ultralow reflection. Nano-Micro Lett. **14**(1), 19 (2021). https://doi.org/10.1007/s40820-021-00759-4

36. G. Sang, P. Xu, T. Yan, V. Murugadoss, N. Naik et al., Interface engineered microcellular magnetic conductive polyurethane nanocomposite foams for electromagnetic interference shielding. Nano-Micro Lett. **13**(1), 153 (2021). https://doi.org/10.1007/s40820-021-00677-5

37. B. Zhao, Y. Li, Q. Zeng, L. Wang, J. Ding et al., Galvanic replacement reaction involving core–shell magnetic chains and orientation-tunable microwave absorption properties. Small **16**(40), 2003502 (2020). https://doi.org/10.1002/smll.202003502

38. M.S. Chang, S.J. Kwon, J.W. Jeong, S.H. Ryu, S.J. Jeong et al., Electromagnetic wave absorbing, thermal-conductive flexible membrane with shape-modulated feco nanobelts. ACS Appl. Mater. Interfaces **14**(34), 39255–39264 (2022). https://doi.org/10.1021/acsami.2c11094

39. M.-S. Jang, M.S. Chang, Y.-T. Kwon, S. Yang, J. Gwak et al., High-throughput thermal plasma synthesis of fexco1−x nanochained particles with unusually high permeability and their electromagnetic wave absorption properties at high frequency (1–26 GHZ). Nanoscale **13**(27), 12004–12016 (2021). https://doi.org/10.1039/D1NR01845K

40. C. Wen, X. Li, R. Zhang, C. Xu, W. You et al., High-density anisotropy magnetism enhanced microwave absorption performance in $Ti_3C_2T_x$ mxene@Ni microspheres. ACS Nano **16**(1), 1150–1159 (2022). https://doi.org/10.1021/acsnano.1c08957

41. Q. Liu, Q. Cao, H. Bi, C. Liang, K. Yuan et al., CoNi@SiO_2@TiO_2 and CoNi@air@TiO_2 microspheres with strong wideband microwave absorption. Adv. Mater. **28**(3), 486–490 (2016). https://doi.org/10.1002/adma.201503149

42. B. Zhao, X. Guo, W. Zhao, J. Deng, G. Shao et al., Yolk–shell Ni@SnO_2 composites with a designable interspace to improve the electromagnetic wave absorption properties. ACS Appl. Mater. Interfaces **8**(42), 28917–28925 (2016). https://doi.org/10.1021/acsami.6b10886

43. R.C. Che, C.Y. Zhi, C.Y. Liang, X.G. Zhou, Fabrication and microwave absorption of carbon nanotubes/$CoFe_2O_4$ spinel nanocomposite. Appl. Phys. Lett. **88**(3), 033105 (2006). https://doi.org/10.1063/1.2165276

44. B. Zhao, Y. Du, Z. Yan, L. Rao, G. Chen et al., Structural defects in phase-regulated high-entropy oxides toward superior microwave absorption properties. Adv. Funct. Mater. **33**(1), 2209924 (2023). https://doi.org/10.1002/adfm.202209924

45. S. Iqbal, G. Kotnala, J. Shah, S. Ahmad, Barium ferrite nanoparticles: a highly effective emi shielding material. Mater. Res. Express. **6**(5), 055018 (2019). https://doi.org/10.1088/2053-1591/ab02a4

46. M. Zahid, S. Siddique, R. Anum, M.F. Shakir, Y. Nawab et al., M-type barium hexaferrite-based nanocomposites for emi shielding application: a review. J. Supercond. Nov. Magn. **34**(4), 1019–1045 (2021). https://doi.org/10.1007/s10948-021-05859-1

47. D. Ratnam, W. Buessem, On the nature of defects in barium ferrite platelets. IEEE Trans. Magn. **6**(3), 610–614 (1970). https://doi.org/10.1109/TMAG.1970.1066877

48. Ü. Özgür, Y. Alivov, H. Morkoç, Microwave ferrites, part 1: fundamental properties. J. Mater. Sci. Mater. Electron. **20**(9), 789–834 (2009). https://doi.org/10.1007/s10854-009-9923-2

49. H. Sözeri, Z. Mehmedi, H. Kavas, A. Baykal, Magnetic and microwave properties of $BaFe_{12}O_{19}$ substituted with magnetic, non-magnetic and dielectric ions. Ceram. Int. **41**(8), 9602–9609 (2015). https://doi.org/10.1016/j.ceramint.2015.04.022

50. H. Sözeri, H. Deligöz, H. Kavas, A. Baykal, Magnetic, dielectric and microwave properties of M-Ti substituted barium hexaferrites (m=Mn^{2+}, Co^{2+}, Cu^{2+}, Ni^{2+}, Zn^{2+}). Ceram. Int. **40**(6), 8645–8657 (2014). https://doi.org/10.1016/j.ceramint.2014.01.082

51. C. Dong, X. Wang, P. Zhou, T. Liu, J. Xie et al., Microwave magnetic and absorption properties of m-type ferrite $BaCo_xTi_xFe_{12-2x}O_{19}$ in the ka band. J. Magn. Magn. Mater. **354**, 340–344 (2014). https://doi.org/10.1016/j.jmmm.2013.11.008

52. C. Liu, Y. Zhang, Y. Tang, Z. Wang, H. Tang et al., Excellent absorption properties of $BaFe_{12-x}Nb_xO_{19}$ controlled by multi-resonance permeability, enhanced permittivity, and the order of matching thickness. Phys. Chem. Chem. Phys. **19**(32), 21893–21903 (2017). https://doi.org/10.1039/C7CP03014B

53. C. Liu, Y. Zhang, Y. Tang, Z. Wang, N. Ma et al., The tunable magnetic and microwave absorption properties of the Nb^{5+}–Ni^{2+} co-doped m-type barium ferrite. J. Mater. Chem. C **5**(14), 3461–3472 (2017). https://doi.org/10.1039/C7TC00393E

54. D. Chen, Y. Liu, Y. Li, K. Yang, H. Zhang, Microstructure and magnetic properties of Al-doped barium ferrite with sodium citrate as chelate agent. J. Magn. Magn. Mater. **337–338**, 65–69 (2013). https://doi.org/10.1016/j.jmmm.2013.02.036

55. C. Liu, Q. Xu, Y. Tang, Z. Wang, R. Ma et al., Zr^{4+} doping-controlled permittivity and permeability of $BaFe_{12-x}Zr_xO_{19}$ and the extraordinary em absorption power in the millimeter wavelength frequency range. J. Mater. Chem. C **4**(40), 9532–9543 (2016). https://doi.org/10.1039/C6TC03430F

56. M. Atif, S. Ullah, A.U. Rehman, K. Shahzad, W. Khalid et al., Structural, magnetic, and dielectric properties of Ti^{4+}−M^{2+}

co-doped BaFe11Ti0.5M0.5O19 hexaferrites (m=Co^{2+}, Ni^{2+}, Zn^{2+}). Ceram. Int. **47**(11), 15245–15252 (2021). https://doi.org/10.1016/j.ceramint.2021.02.087

57. E.A. Gorbachev, L.A. Trusov, L.N. Alyabyeva, I.V. Roslyakov, V.A. Lebedev et al., High-coercivity hexaferrite ceramics featuring sub-terahertz ferromagnetic resonance. Mater. Horiz. **9**(4), 1264–1272 (2022). https://doi.org/10.1039/D1MH01797G

58. L.A. Trusov, E.A. Gorbachev, V.A. Lebedev, A.E. Sleptsova, I.V. Roslyakov et al., Ca–Al double-substituted strontium hexaferrites with giant coercivity. Chem. Commun. **54**(5), 479–482 (2018). https://doi.org/10.1039/C7CC08675J

59. E.A. Gorbachev, L.A. Trusov, A.E. Sleptsova, E.S. Kozlyakova, L.N. Alyabyeva et al., Hexaferrite materials displaying ultra-high coercivity and sub-terahertz ferromagnetic resonance frequencies. Mater. Today **32**, 13–18 (2020). https://doi.org/10.1016/j.mattod.2019.05.020

60. H. Li, L. Zheng, D. Deng, X. Yi, X. Zhang et al., Multiple natural resonances broaden microwave absorption bandwidth of substituted m-type hexaferrites. J. Alloys Compd. **862**, 158638 (2021). https://doi.org/10.1016/j.jallcom.2021.158638

61. Y. Guan, Y. Lin, L. Zou, Q. Miao, M. Zeng et al., The effects of Co-Ti co-doping on the magnetic, electrical, and magnetodielectric behaviors of m-type barium hexaferrites. AIP Adv. **3**(12), 122115 (2013). https://doi.org/10.1063/1.4860948

62. A. Nicolson, G. Ross, Measurement of the intrinsic properties of materials by time-domain techniques. IEEE Trans. Instrum. Meas. **19**(4), 377–382 (1970). https://doi.org/10.1109/TIM.1970.4313932

63. Z. Wang, M. Yang, B. Zheng, P. Wang, Y. Wang et al., Tunable magnetization of single domain m-type barium hexagonal ferrite nano powders by Co–Ti substitution via chemical co-precipitation plus molten salts method. Ceram. Int. **48**((19 Part A)), 27779–27784 (2022). https://doi.org/10.1016/j.ceramint.2022.06.079

64. Y. Slimani, M.A. Almessiere, S. Guner, A. Baykal, M. Sertkol et al., An investigation on structural, optical and magnetic properties of hard-soft $SrFe_{12}O_{19}/(CoEu_{0.02}Fe_{1.98}O_4)_x$ nanofiber composites. J. Alloys Compd **905**, 164240 (2022). https://doi.org/10.1016/j.jallcom.2022.164240

65. G.A. Alnawashi, A.M. Alsmadi, I. Bsoul, G.M. Alzoubi, B. Salameh et al., Magnetic study of m-type Co-Ti doped strontium hexaferrite nanocrystalline particles. J. Supercond. Nov. Magn. **33**(5), 1423–1432 (2020). https://doi.org/10.1007/s10948-019-05334-y

66. L. Shao, A. Sun, Y. Zhang, L. Yu, N. Suo et al., Microstructure, xps and magnetic analysis of Al-doped nickel–manganese–cobalt ferrite. J. Mater. Sci. Mater. Electron. **32**(15), 20474–20488 (2021). https://doi.org/10.1007/s10854-021-06557-3

67. R.C. Pullar, Hexagonal ferrites: a review of the synthesis, properties and applications of hexaferrite ceramics. Prog. Mater. Sci. **57**(7), 1191–1334 (2012). https://doi.org/10.1016/j.pmatsci.2012.04.001

68. X.Z. Zhou, A.H. Morrish, Z.W. Li, Y.K. Hong, Site preference for Co^{2+} and Ti^{4+}/ in Co-Ti substituted barium ferrite. IEEE Trans. Magn. **27**(6), 4654–4656 (1991). https://doi.org/10.1109/20.278906

69. J.M. Williams, J. Adetunji, M. Gregori, Mössbauer spectroscopic determination of magnetic moments of Fe^{3+} and Co^{2+} in substituted barium hexaferrite, $Ba(Co, Ti)xF_{e(12-2x)}O19$. J. Magn. Magn. Mater. **220**(2), 124–128 (2000). https://doi.org/10.1016/S0304-8853(00)00458-3

70. S.Y. An, I.-B. Shim, C.S. Kim, Mössbauer and magnetic properties of Co–Ti substituted barium hexaferrite nanoparticles. J. Appl. Phys. **91**(10), 8465–8467 (2002). https://doi.org/10.1063/1.1452203

71. A.G. Belous, O.I. V'Yunov, E.V. Pashkova, V.P. Ivanitskii, O.N. Gavrilenko, Mössbauer study and magnetic properties of m-type barium hexaferrite doped with Co + Ti and Bi + Ti ions. J. Phys. Chem. B **110**(51), 26477–26481 (2006). https://doi.org/10.1021/jp064628t

72. M. Przybylski, J. Żukrowski, I. Harward, Z. Celiński, Mössbauer spectroscopy study of Al distribution in $BaAl_xFe_{12-x}O_{19}$ thin films. J. Appl. Phys. **117**(17), 17A501 (2015). https://doi.org/10.1063/1.4914359

73. D.H. Choi, S.Y. An, S.W. Lee, I.-B. Shim, C.S. Kim, Site occupancy and anisotropy distribution of al substituted baferrite with high coercivity. Phys. Status Solidi B **241**(7), 1736–1739 (2004). https://doi.org/10.1002/pssb.200304633

74. V. Dixit, C.N. Nandadasa, S.-G. Kim, S. Kim, J. Park et al., Site occupancy and magnetic properties of Al-substituted m-type strontium hexaferrite. J. Appl. Phys. **117**(24), 243904 (2015). https://doi.org/10.1063/1.4922867

75. J.N. Dahal, L. Wang, S.R. Mishra, V.V. Nguyen, J.P. Liu, Synthesis and magnetic properties of $SrFe_{12-x-y}Al_xCO_yO_{19}$ nanocomposites prepared via autocombustion technique. J. Alloys Compd. **595**, 213–220 (2014). https://doi.org/10.1016/j.jallcom.2013.12.186

76. M. Zhang, Q. Liu, G. Zhu, S. Xu, Magnetic properties of co and ti co-doped strontium hexaferrite prepared by sol–gel method. Appl. Phys. A **125**(3), 191 (2019). https://doi.org/10.1007/s00339-019-2500-5

77. J. Kreisel, H. Vincent, F. Tasset, M. Paté, J.P. Ganne, An investigation of the magnetic anisotropy change in $BaFe_{12}-2xTi_xCo_xO_{19}$ single crystals. J. Magn. Magn. Mater. **224**(1), 17–29 (2001). https://doi.org/10.1016/S0304-8853(00)01355-X

78. G. Han, R. Sui, Y. Yu, L. Wang, M. Li et al., Structure and magnetic properties of the porous Al-substituted barium hexaferrites. J. Magn. Magn. Mater. **528**, 167824 (2021). https://doi.org/10.1016/j.jmmm.2021.167824

79. N.-N. Song, Y.-J. Ke, H.-T. Yang, H. Zhang, X.-Q. Zhang et al., Integrating giant microwave absorption with magnetic refrigeration in one multifunctional intermetallic compound of lafe (11.6)Si(1.4)C(0.2)H(1.7). Sci. Rep. **3**, 2291 (2013). https://doi.org/10.1038/srep02291

80. P.M. Gradzki, F.C. Lee, Domain wall resonance and its effect on losses in ferrites. PESC 91 Rec. 22nd Annu. IEEE

Power Electr. Spec. Conf. (1991). https://doi.org/10.1109/PESC.1991.162741

81. Y. Yin, M. Zeng, J. Liu, W. Tang, H. Dong et al., Enhanced high-frequency absorption of anisotropic Fe_3O_4/graphene nanocomposites. Sci. Rep. **6**, 25075 (2016). https://doi.org/10.1038/srep25075

82. J. Qiu, M. Gu, H. Shen, Microwave absorption properties of Al- and Cr-substituted m-type barium hexaferrite. J. Magn. Magn. Mater. **295**(3), 263–268 (2005). https://doi.org/10.1016/j.jmmm.2005.01.018

83. M. Jazirehpour, M.H. Shams, O. Khani, Modified sol–gel synthesis of nanosized magnesium titanium substituted barium hexaferrite and investigation of the effect of high substitution levels on the magnetic properties. J. Alloys Compd. **545**, 32–40 (2012). https://doi.org/10.1016/j.jallcom.2012.08.043

84. X.Z. Zhou, A.H. Morrish, Z. Yang, H.X. Zeng, Co-sn substituted barium ferrite particles. J. Appl. Phys. **75**(10), 5556–5558 (1994). https://doi.org/10.1063/1.355687

85. Y. Xu, G.L. Yang, D.P. Chu, H.R. Zhai, Magnetic anisotropy of bam ferrites. J. Magn. Magn. Mater. **31–34**, 815–816 (1983). https://doi.org/10.1016/0304-8853(83)90699-6

86. J. Zhang, Y. Xie, H. Xu, T. Zhou, Efficient and simple fabrication of high-strength and high-conductivity metallization patterns on flexible polymer films. Ind. Eng. Chem. Res. **61**(20), 6987–6996 (2022). https://doi.org/10.1021/acs.iecr.2c00850

87. Y. Naito, K. Suetake, Application of ferrite to electromagnetic wave absorber and its characteristics. IEEE Trans. Microw. Theory Techn. **19**(1), 65–72 (1971). https://doi.org/10.1109/TMTT.1971.1127446

88. D. Zhou, X. Huang, Z. Du, Analysis and design of multilayered broadband radar absorbing metamaterial using the 3-d printing technology-based method. IEEE Antennas Wirel. Propag. Lett. **16**, 133–136 (2017). https://doi.org/10.1109/LAWP.2016.2560904

89. G. Wang, Y. Zhao, F. Yang, Y. Zhang, M. Zhou et al., Multifunctional integrated transparent film for efficient electromagnetic protection. Nano-Micro Lett. **14**(1), 65 (2022). https://doi.org/10.1007/s40820-022-00810-y

90. T. Kim, J. Lee, K. Lee, B. Park, B.M. Jung et al., Magnetic and dispersible feconi-graphene film produced without heat treatment for electromagnetic wave absorption. Chem. Eng. J. **361**, 1182–1189 (2019). https://doi.org/10.1016/j.cej.2018.12.172

91. Z. Jiao, W. Huyan, F. Yang, J. Yao, R. Tan et al., Achieving ultra-wideband and elevated temperature electromagnetic wave absorption via constructing lightweight porous rigid structure. Nano-Micro Lett. **14**(1), 173 (2022). https://doi.org/10.1007/s40820-022-00904-7

92. W.B. Weir, Automatic measurement of complex dielectric constant and permeability at microwave frequencies. Proc. IEEE **62**(1), 33–36 (1974). https://doi.org/10.1109/PROC.1974.9382

93. L.D.C. Folgueras, E.L. Nohara, R. Faez, M.C. Rezende, Dielectric microwave absorbing material processed by impregnation of carbon fiber fabric with polyaniline. Mater. Res. **10**(1), 95–99 (2007). https://doi.org/10.1590/S1516-14392007000100020

94. Advanced antenna systems for 5g. 5G Americas White Papers. (2019)

95. A. Narayanan, M.I. Rochman, A. Hassan, B.S. Firmansyah, V. Sathya et al., A comparative measurement study of commercial 5g mmwave deployments. IEEE INFOCOM 2022 IEEE Conf. Comput. Commun. (2022). https://doi.org/10.1109/INFOCOM48880.2022.9796693

96. J. Hasch, E. Topak, R. Schnabel, T. Zwick, R. Weigel et al., Millimeter-wave technology for automotive radar sensors in the 77 ghz frequency band. IEEE Trans. Microw. Theory Techn. **60**(3), 845–860 (2012). https://doi.org/10.1109/TMTT.2011.2178427

97. A. Lazaro, M. Lazaro, R. Villarino, D. Girbau, Seat-occupancy detection system and breathing rate monitoring based on a low-cost mm-wave radar at 60 ghz. IEEE Access. **9**, 115403–115414 (2021). https://doi.org/10.1109/ACCESS.2021.3105390

98. J. Tolvanen, J. Hannu, M. Hietala, K. Kordas, H. Jantunen, Biodegradable multiphase poly(lactic acid)/biochar/graphite composites for electromagnetic interference shielding. Compos. Sci. Technol. **181**, 107704 (2019). https://doi.org/10.1016/j.compscitech.2019.107704

99. G. Han, Z. Ma, B. Zhou, C. He, B. Wang et al., Cellulose-based ni-decorated graphene magnetic film for electromagnetic interference shielding. J. Colloid Interface Sci. **583**, 571–578 (2021). https://doi.org/10.1016/j.jcis.2020.09.072

100. H. Cheng, S. Wei, Y. Ji, J. Zhai, X. Zhang et al., Synergetic effect of fe3o4 nanoparticles and carbon on flexible poly (vinylidence fluoride) based films with higher heat dissipation to improve electromagnetic shielding. Compos. A Appl. Sci. Manuf. **121**, 139–148 (2019). https://doi.org/10.1016/j.compositesa.2019.03.019

101. S.S. Chauhan, M. Verma, P. Verma, V.P. Singh, V. Choudhary, Multiwalled carbon nanotubes reinforced poly (etherketone) nanocomposites: Assessment of rheological, mechanical, and electromagnetic shielding properties. Polym. Adv. Technol. **29**(1), 347–354 (2018). https://doi.org/10.1002/pat.4120

102. S.-Y. Liao, G. Li, X.-Y. Wang, Y.-J. Wan, P.-L. Zhu et al., Metallized skeleton of polymer foam based on metal–organic decomposition for high-performance emi shielding. ACS Appl. Mater. Interfaces. **14**(2), 3302–3314 (2022). https://doi.org/10.1021/acsami.1c21836

103. Z. Wang, Q.-Q. Kong, Z.-L. Yi, L.-J. Xie, H. Jia et al., Electromagnetic interference shielding material for super-broadband: Multi-walled carbon nanotube/silver nanowire film with an ultrathin sandwich structure. J. Mater. Chem. A. **9**(46), 25999–26009 (2021). https://doi.org/10.1039/D1TA08106C

104. X.Y. Wang, S.Y. Liao, Y.J. Wan, H.P. Huang, X.M. Li et al., Near-field and far-field emi shielding response of lightweight and flexible mxene-decorated polyester textiles. Mater. Today Phys. **23**, 100644 (2022). https://doi.org/10.1016/j.mtphys.2022.100644

105. K.K. Halder, M. Tomar, V.K. Sachdev, V. Gupta, Development of polyvinylidene fluoride–graphite composites as an alternate material for electromagnetic shielding applications. Mater. Res. Express. **6**(7), 075324 (2019). https://doi.org/10.1088/2053-1591/ab13dd

106. L. Vovchenko, L. Matzui, V. Oliynyk, V. Launets, Y. Mamunya et al., Nanocarbon/polyethylene composites with segregated conductive network for electromagnetic interference shielding. Mol. Cryst. Liq. Cryst. **672**(1), 186–198 (2018). https://doi.org/10.1080/15421406.2018.1555349

107. N. Vohra, M. El-Shenawee, K- and w-band free-space characterizations of highly conductive radar absorbing materials. IEEE Trans. Instrum. Meas. **70**, 1–10 (2021). https://doi.org/10.1109/TIM.2020.3041821

108. BASF. Ultradur® rx (pbt). (2022)

109. W.-L. Song, X.-T. Guan, L.-Z. Fan, W.-Q. Cao, C.-Y. Wang et al., Magnetic and conductive graphene papers toward thin layers of effective electromagnetic shielding. J. Mater. Chem. A. **3**(5), 2097–2107 (2015). https://doi.org/10.1039/C4TA05939E

110. L.-Q. Zhang, B. Yang, J. Teng, J. Lei, D.-X. Yan et al., Tunable electromagnetic interference shielding effectiveness via multilayer assembly of regenerated cellulose as a supporting substrate and carbon nanotubes/polymer as a functional layer. J Mater. Chem. C **5**(12), 3130–3138 (2017). https://doi.org/10.1039/C6TC05516H